Focal seizures are organized by feedback between neural activity and ion concentration changes

Damiano Gentiletti,[1] Marco de Curtis,[2] Vadym Gnatkovsky,[2,3] and Piotr Suffczynski,[1*]

Author affiliations:

1 Department of Biomedical Physics, Faculty of Physics, University of Warsaw, 02-093 Warsaw, Poland

2 Epilepsy Unit, Fondazione IRCCS Istituto Neurologico *Carlo Besta*, 20133 Milan, Italy

3 Department of Epileptology, University Hospital Bonn, 53127 Bonn, Germany

[*]Corresponding author: suffa@fuw.edu.pl

Abstract

Human and animal EEG data demonstrate that focal seizures start with low-voltage fast activity, evolve into rhythmic burst discharges and are followed by a period of suppressed background activity. This suggests that processes with dynamics in the range of tens of seconds govern focal seizure evolution. We investigate the processes associated with seizure dynamics by complementing the Hodgkin-Huxley mathematical model with the physical laws that dictate ion movement and maintain ionic gradients. We show that the disturbance of K^+ and Cl^- homeostasis by the fast discharge of inhibitory interneurons is sufficient to initiate seizures, which are maintained by positive feedback between ion concentration changes and neuronal activity. Gradual Na^+ accumulation increases the rate of the Na^+/K^+-pump, creating negative feedback which slows down and terminates ictal discharges and contributes to the postictal state. Our results emphasize ionic dynamics as elementary processes behind seizure generation and indicate targets for new therapeutic strategies.

Introduction

Focal seizure patterns recorded with intracranial and intracerebral electrodes in patients submitted to presurgical evaluation often consist of distinct phases (Franaszczuk et al., 1998; Spencer et al., 1992; Velascol et al., 2000). A frequently observed onset pattern in patients with temporal lobe epilepsy (TLE) is characterized by low-voltage fast (LVF) activity in the gamma range (30–80 Hz) (Avoli et al., 2016; de Curtis & Gnatkovsky, 2009; Lagarde et al., 2019; Perucca et al., 2014). LVF seizure onset is followed by the recruitment of irregular spiking behavior which evolves into periodic burst discharges that gradually decrease in frequency and suddenly cease. Seizures are often followed by a period of reduced EEG amplitude known as postictal EEG suppression. The traditional view on epileptic seizures is that they result from an imbalance of synaptic excitation and inhibition (Bradford, 1995; Bragin et al., 2009). It is unclear how this concept may account for the electroencephalographic complexity of TLE seizures and their characteristic progression from one phase to the next. The findings of several studies have not confirmed the role of synaptic interaction in seizure generation or progression. It has been shown that blocking synaptic transmission via a low Ca^{2+} solution led to the development of synchronized seizure-like events (SLE) in hippocampal CA1 slices (Jefferys & Haas, 1982; Yaari et al., 1983) and in the intact hippocampus (Feng & Durand, 2003). Moreover, the synchronized epileptiform activity can be recorded across two hippocampal regions separated by a mechanical lesion, without the involvement of electrochemical synaptic communication (Lian et al., 2001). Finally, in photosensitive baboons, light-induced neocortical seizure discharges were accompanied by depletion of extracellular Ca^{2+} to levels incompatible with the chemical synaptic transmission (Pumain et al., 1985). Additionally, a paradoxical increase in inhibitory cell firing and a decrease in pyramidal cell activity at seizure onset was documented in *in vitro* rodent slices (Derchansky et al., 2008; Fujiwara-Tsukamoto et al., 2007; Lévesque et al., 2016; Lillis et al., 2012; Ziburkus et al., 2006), in the *in vitro* whole guinea pig brain (Gnatkovsky et al., 2008; Uva et al., 2015), and in human and animal *in vivo* recordings (Elahian et al., 2018; Grasse et al., 2013; Miri et al., 2018; Toyoda et al., 2015; Truccolo et al., 2011). The above-mentioned studies suggest that processes at the network level related to changes in synaptic gains cannot be the sole mechanisms that control seizure generation and progression, and that other factors must be involved in the process of ictogenesis.

Although several non-synaptic mechanisms have been proposed to influence abnormal synchronization (Blauwblomme et al., 2014; de Curtis et al., 2018; Jefferys et al., 2012;

Raimondo et al., 2015), the specific mechanisms responsible for seizure induction, evolution and termination remain unclear. In the present study, we investigated the possible mechanisms of the LVF seizure pattern using a realistic computational model of the hippocampal network that included activity-dependent ion concentration changes. We based our simulations on the data recorded in the *in vitro* isolated guinea pig brain preparation, which is an animal model of human temporal lobe seizures (de Curtis et al., 2006; de Curtis & Gnatkovsky, 2009). We used these experimental recordings to guide our *in silico* study due to the availability of data at the network, cellular and ionic levels. A computer model was used to demonstrate that seizures initiated via increased interneuron discharges, evolved, and terminated autonomously due to activity-dependent ion concentration shifts and homeostatic mechanisms that worked continuously to restore physiological transmembrane ion levels. Our modelling results suggest a link between the seizure termination mechanism and postictal suppression state and predict a specific scaling law of inter-bursting intervals observed at the end of seizures, which was validated experimentally.

Results

The model consisted of five cells, four pyramidal neurons (PY) and a fast-spiking inhibitory interneuron (IN), arranged as a chain structure (Fig. 1). The ionic dynamics of K^+, Na^+, Ca^{2+} and Cl^- were incorporated and activity-dependent changes in their concentrations were computed. Concentration changes in each extracellular or intracellular compartment were dependent on several mechanisms such as active and passive membrane currents, inhibitory synaptic GABAa currents, Na^+/K^+-pump, KCC2 cotransporter, glial K^+ buffer, Ca^{2+} pump and buffer, radial diffusion, longitudinal diffusion and volume changes. Additionally, we included impermeant anions (A^-) with concentration dependent volume changes and bicarbonate ions (HCO_3^-) that contributed to GABAa currents.

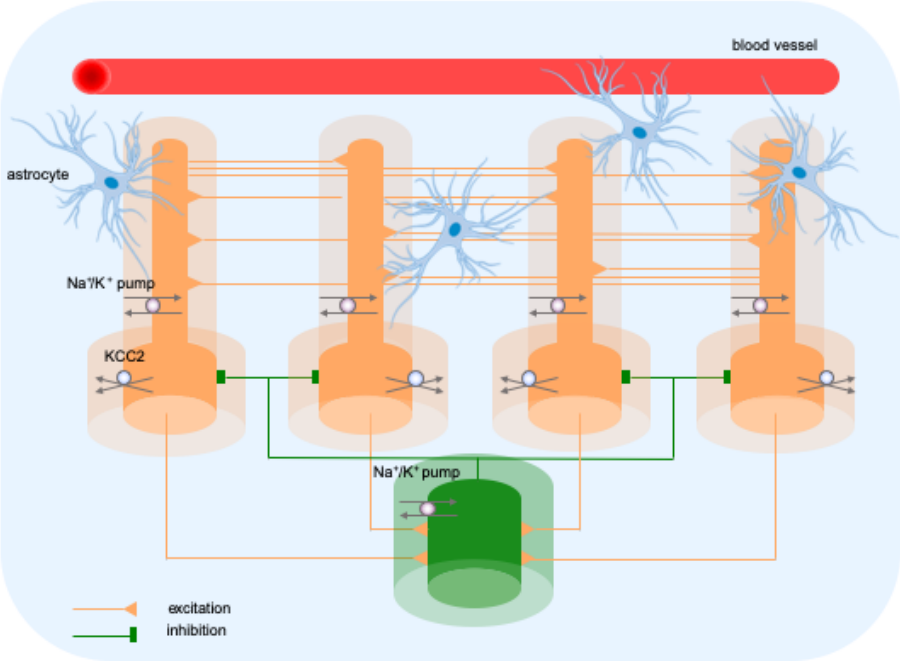

Figure 1. Model diagram. The model consisted of four pyramidal cells (orange) and an interneuron (green) linked by excitatory (AMPA) and inhibitory (GABAa) synaptic connections. Each cellular compartment was surrounded by an interstitial compartment. The interstitial space was enclosed in a common bath (blue) which represented the surrounding tissue and vasculature not included in the model. The model included variable intracellular and extracellular ion concentrations computed according to ionic currents flowing across neuronal membranes, longitudinal diffusion between the dendritic and somatic compartments, radial diffusion between neighboring interstitial compartments and diffusion to/from the bath. Additionally, the model included ionic regulation mechanisms: a Na^+/K^+-pump, a KCC2 cotransporter and K^+ buffering by astrocytes.

Three phases of an LVF onset SLE

A simulated SLE emerging from normal background activity is shown in Fig. 2. To test the hypothesis that the onset of focal seizures is associated with an increased discharge of IN (de Curtis & Avoli, 2016), we applied a depolarizing current (Fig. 2C, yellow trace) to the IN at second 60. Strong firing (initial rate of 270 Hz) of the IN (Fig. 2C) led to small amplitude fast activity in the LFP signal (Fig. 2A between the 60 and 65-second timestamps) associated with the onset of the simulated SLE. After approximately 10 seconds, the PY cells began to generate a strong tonic discharge, resulting in an irregular LFP spiking signal with increased amplitude typically associated with the SLE tonic phase (Fig. 2B; 65–80 seconds). Approximately 15–20

seconds after the onset of the SLE, the cellular firing pattern of PY cells switched from tonic to bursting discharge, leading to LFP oscillations which corresponded to the bursting phase (Fig. 2A, after 80 seconds). As the SLE progressed, the burst rate gradually decreased and ictal discharges spontaneously terminated. Postictally, the SLE was followed by a period of silence for approximately 30 seconds which was visible in the LFP signal and in the PY and IN traces (Fig. 2A–C). After the postictal depression, the background firing reappeared and gradually returned to a baseline level. The SLE discharges were accompanied by significant changes in the intracellular and extracellular ionic concentrations. At the onset of the seizure, extracellular potassium concentration ($[K^+]_o$) increased sharply in the somatic compartment, remained elevated throughout the SLE and slightly decreased toward the end of the episode (Fig. 2D). Intracellular sodium concentration ($[Na^+]_i$) steadily increased during the bursting phase in both somatic and dendritic compartments and reached a plateau around the offset of the SLE (Fig. 2E). Intracellular chloride concentration ($[Cl^-]_i$) exhibited a gradual increase from the beginning of the SLE and was highest at the end of the paroxysmal firing (Fig. 2F).

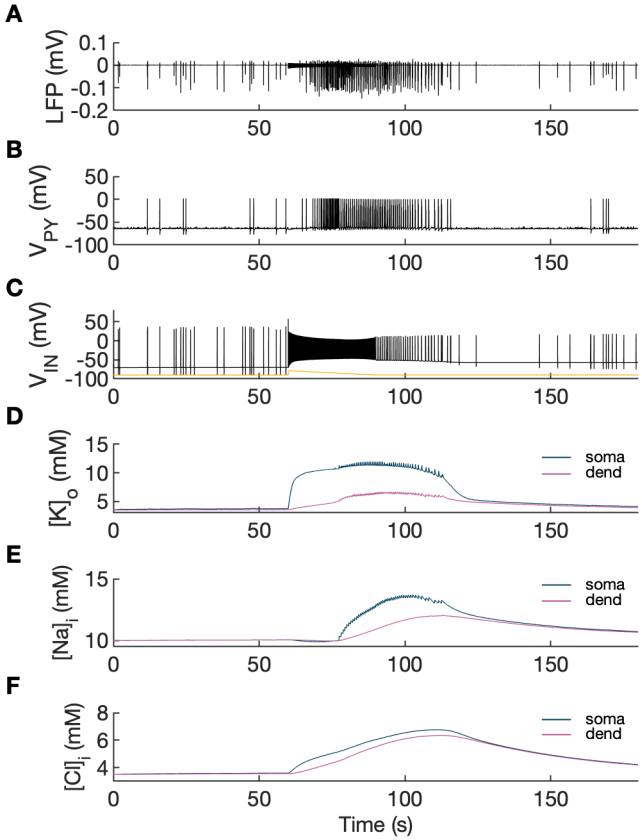

Figure 2. Model behavior during an SLE. (A) Local field potential (LFP) signal. **(B)** Pyramidal cell (PY) membrane potential. **(C)** Interneuron (IN) membrane potential. **(D)**

Extracellular potassium concentration. **(E)** Intracellular sodium concentration. **(F)** Intracellular chloride concentration. In the interictal phase (0–60 seconds), the model generated irregular background firing and the ion concentrations were at their resting values (**A–F**). The current injected into the interneuron at second 60 (**C**, yellow) triggered fast IN spiking (**C**, black) which also manifested as low voltage fast activity in the LFP signal (**A**). Approximately 10 seconds after the initiation of the SLE, PY cells initiated tonic firing that subsequently shifted to bursting (**B**). The behavior of the PY cells was reflected in the LFP trace which showed irregular activity and synchronized bursting (**A**). The SLE terminated at approximately second 120 and was followed by a period of reduced excitability (**A–C**). The cellular activity was accompanied by significant ion concentration shifts. Extracellular potassium in the somatic compartment increased sharply and remained elevated throughout the SLE (**D**, dark blue). The $[K^+]_o$ increase in the dendritic compartment was slower and less pronounced (**D**, violet). The intracellular sodium increased gradually toward a plateau (**E**). The intracellular chloride accumulated steadily throughout the SLE (**F**).

A comparison of the simulation results with the available experimental data is shown in Fig. 3. In the isolated guinea pig brain, the SLE activity with an LVF onset pattern (Fig. 3A, top trace) was induced by the arterial application of bicuculine. The transition from preictal to ictal state which occurred at approximately second 10 was associated with a strong discharge of fast-spiking interneurons (Fig. 3A, third trace) and transient silencing of the PY cells (Fig. 3A, second trace). The strong preictal firing of the PY cells was artificially triggered by the injection of a steady depolarizing current via the intracellular recording electrode to analyze the intracellular firing correlates during the SLE (Gnatkovsky et al., 2008). Within a few seconds from the initiation of the sustained interneuron discharge, the principal PY cells were recruited first into tonic firing and subsequently into bursting discharges which were visible in the PY membrane potential and LFP signals. $[K^+]_o$ sharply increased at the onset of the SLE and remained elevated afterward (Fig. 3A, bottom trace). The *in silico* results (shown for comparison in the same timescale in Fig. 3B) replicated the experimental data in many respects including LFP signal characteristics, cellular firing pattern and $[K^+]_o$ time course.

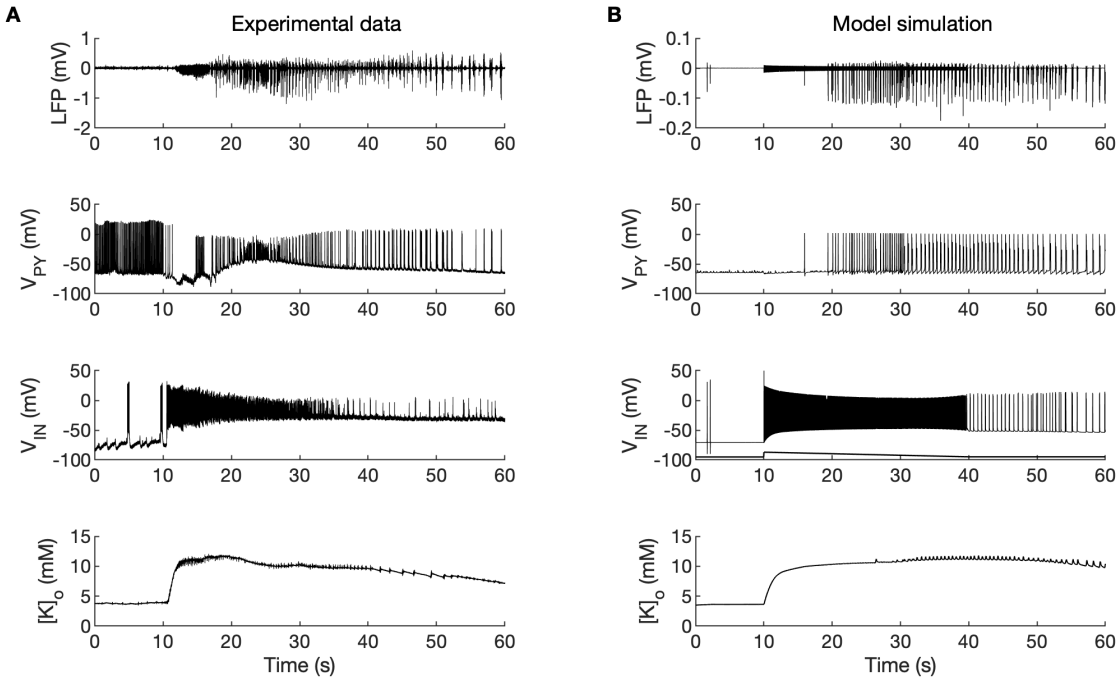

Figure 3. A comparison between the experimental data and the model simulation. (A) Experimental recordings of a seizure-like event (SLE) in the *in vitro* isolated whole guinea pig brain preparation (de Curtis et al., 2006; Gnatkovsky et al., 2008; Uva et al., 2015). From top to bottom: LFP signal, intracellular recording of pyramidal cell (PY) and interneuron (IN), extracellular potassium. The onset of the SLE was associated with increased IN firing, silencing PY and low-voltage fast (LVF) activity in the LFP signal. Approximately 10 seconds after the onset of the SLE, the PY exhibited a tonic and then burst firing behavior. The extracellular potassium increased up to approximately 10 mM at the onset of the SLE and remained elevated afterward. **(B)** The activity patterns in the LFP signal, pyramidal cells, interneuron and $[K^+]_o$ were reproduced accurately by the model except for preictal firing of the PY cell seen in **A**, which was artificially depolarized above resting membrane potential to highlight the role of the inhibitory interneurons during the SLE (Gnatkovsky et al., 2008).

In the simulations, the excitatory and inhibitory synaptic conductances were "clamped" throughout the entire simulation period, hence, they could not contribute to the progression from one phase to another. Conversely, variations in ion concentrations were expected to affect neuronal excitability. For example, an increase in $[K^+]_o$ reduces the driving force of K^+ currents responsible for hyperpolarized resting membrane potential and spike repolarization. $[Na^+]_i$ and $[K^+]_o$ affect the rate of the Na^+/K^+-pump that transports three Na^+ ions out of the cell for every two K^+ ions pumped into the cell, thus producing an outward current. Accumulation of $[K^+]_o$ and

$[Na^+]_i$ increases the pump rate and enhances the hyperpolarizing pump current. Hence, to determine the intrinsic mechanism that modulates excitability, we first investigated the behavior of the model in response to variations in extracellular potassium and intracellular sodium concentrations.

The effects of $[K^+]_o$ and $[Na]_i$ on the network model

Activity-dependent changes in ion concentrations are slow compared to neuronal dynamics, which are relatively fast. To analyze such a system, with slow and fast timescales, it is possible to decouple the fast variables (e.g., membrane potential) from the slow variables (e.g., ionic concentrations). Accordingly, to analyze the role of $[K^+]_o$ and $[Na^+]_i$ in shaping single-cell and network dynamics, we disabled all mechanisms controlling ionic concentrations and analyzed the behavior of the model for different values of $[K^+]_o$ and $[Na^+]_i$. The values of these variables were modified externally and treated as control parameters. In the single cell analysis, all synaptic connections were removed. In the network analysis, all synaptic connections were intact except afferent excitatory input, which was removed from PY cells to eliminate the stochastic component from the analysis; depolarizing current injection was removed from the interneuron. The behavior of a single PY cell was analyzed for different values of extracellular potassium in the dendritic ($[K^+]_{o,dend}$) and somatic compartments ($[K^+]_{o,soma}$). During the analysis, for each fixed value of $[K^+]_{o,dend}$, we performed simulations when sweeping the $[K^+]_{o,soma}$ value from 3 mM to 14 mM (in steps of 0.25 mM) in the forward and backward direction. The initial conditions for each $[K^+]_{o,soma}$ corresponded to the final states in the previous step. For each $[K^+]_{o,soma}$ step, we simulated 5 seconds of activity. After a full sweep with all $[K^+]_{o,soma}$ steps in both directions, the $[K^+]_{o,dend}$ was increased and the analysis was repeated. The analysis was performed for the $[K^+]_{o,dend}$ values in the range of 3–7 mM, in steps of 0.5 mM (or 0.25 mM if a better resolution was required). We found that the behavior of the single cell and network models was the same for increasing and decreasing steps of $[K^+]_{o,soma}$ with small domains of bistability not larger than one step (0.25 mM) between the activity phases. Analysis of the dynamics of a single isolated cell for a reference value of $[Na^+]_i$ at 10 mM can be found in Supplementary material (Fig. S1). In the network analysis, a full sweep with all $[K^+]_{o,soma}$ and $[K^+]_{o,dend}$ steps (as described above) was performed for three different values of $[Na^+]_i$, namely, 10 mM, 11 mM and 12 mM. We assumed, that $[Na^+]_i$ in the dendritic and somatic compartments were equal. In the model simulation shown in Fig. 2E, $[Na^+]_{i,dend}$ values were lower than $[Na^+]_{i,soma}$ values. Accordingly, our assumption may have led to an overestimation of $[Na^+]_{i,dend}$ and the dendritic

199 Na^+/K^+-pump current. The analysis results are shown in Fig. 4A, in which the various activity
200 patterns, i.e., rest, tonic firing and bursting are color-coded (shown on the right). A comparison
201 of the network activities for different values of $[Na^+]_i$ in the three graphs in Fig. 4A demonstrates
202 that the main effect of an increase in $[Na^+]_i$ was a shrinking of the tonic and bursting domains
203 and an expansion of the resting domain due to upregulation of the hyperpolarizing effect of
204 increased $[Na^+]_i$ on the pump current.

205 **The evolution of the SLE mediated by $[K^+]_o$ and $[Na]_i$**

206 In the previous section, the influence of $[K^+]_o$ and $[Na]_i$ on network behavior was examined
207 without accounting for the time factor. Here, we present a fast-slow system analysis approach
208 that considers the time evolution of ionic concentrations, as shown in Fig. 2. Hence, we assessed
209 the dependence of the evolution of an SLE on externally manipulated changes in $[K^+]_o$ and $[Na]_i$
210 with fixed concentrations of all other ions. To obtain improved affinity with the reference
211 simulation (Fig. 2), the chloride concentration in the dendritic compartment of the PY cells was
212 set to 7.5 mM, which corresponded to its peak value during the SLE (Fig. 2F). To schematically
213 describe the extracellular potassium time course from preictal to postictal state (as shown in Fig.
214 2D), we identified four distinct stages (as shown in Fig. 4B top panel): I) a sharp increase in
215 $[K^+]_{o,soma}$, II) elevated $[K^+]_{o,soma}$, a slow increase in $[K^+]_{o,dend}$, III) elevated $[K^+]_{o,dend}$, a slow
216 decrease in $[K^+]_{o,soma}$, IV) a decrease in $[K^+]_{o,soma}$ and $[K^+]_{o,dend}$ back to their resting values.
217 Variations in potassium concentrations were accompanied by changes in $[Na^+]_i$ (Fig. 2E). In the
218 preictal period and during the SLE tonic firing phase, $[Na^+]_i$ in the soma and dendrite was stable,
219 while it increased during the burst firing phase and reached a plateau toward the end of the
220 episode. In the postictal period, $[Na^+]_i$ in both compartments slowly returned to the initial value.
221 The time course of $[Na^+]_i$ approximating intracellular somatic sodium evolution is shown in Fig.
222 4B (middle panel). For simplicity, we assumed that these depicted $[Na^+]_i$ variations were the
223 same in the dendritic and somatic compartments. The corresponding representative PY cell
224 activity is shown in Fig. 4B (bottom trace). To distinguish different SLE phases, the PY cell
225 activity pattern was marked using a color-code, as in Fig. 4A. As $[K^+]_o$ and $[Na^+]_i$ followed their
226 predefined time course, PY cells exhibited transitions from rest to tonic firing, progressed into
227 bursting with a slowing-down pattern and eventually returned to the resting state. In the postictal
228 period (after stage IV), the $[Na^+]_i$ remained elevated for approximately 40 seconds (Fig. 4B
229 middle panel) giving rise to an enhanced hyperpolarizing Na^+/K^+-pump current that reduced the
230 excitability of the network and contributed to postictal depression, as described in the last

paragraph (Fig. 7). To further observe the time evolution of the SLE in the $[K^+]_{o,soma}$, $[K^+]_{o,dend}$ parameter space, we superimposed potassium changes on the bifurcation diagrams in Fig. 4A. The distinct stages of the potassium time course are marked by arrows. The crossing of a border by an arrow corresponds to a transition between different firing regimes. The initial increase of somatic $[K^+]_o$ (stage I) led to a transition from the resting state to tonic firing (Fig. 4A, first panel), while a subsequent increase of dendritic $[K^+]_o$ (stage II) led to a transition from tonic firing to bursting (Fig. 4A, middle panel). A subsequent decrease in somatic $[K^+]_o$ (stage III) led to the termination of the SLE, as the cell activity reentered the resting state region (Fig. 4A, last panel). After termination of the SLE, $[K^+]_{o,soma}$ and $[K^+]_{o,dend}$ returned to their resting values (stage IV in Fig. 4A, last panel).

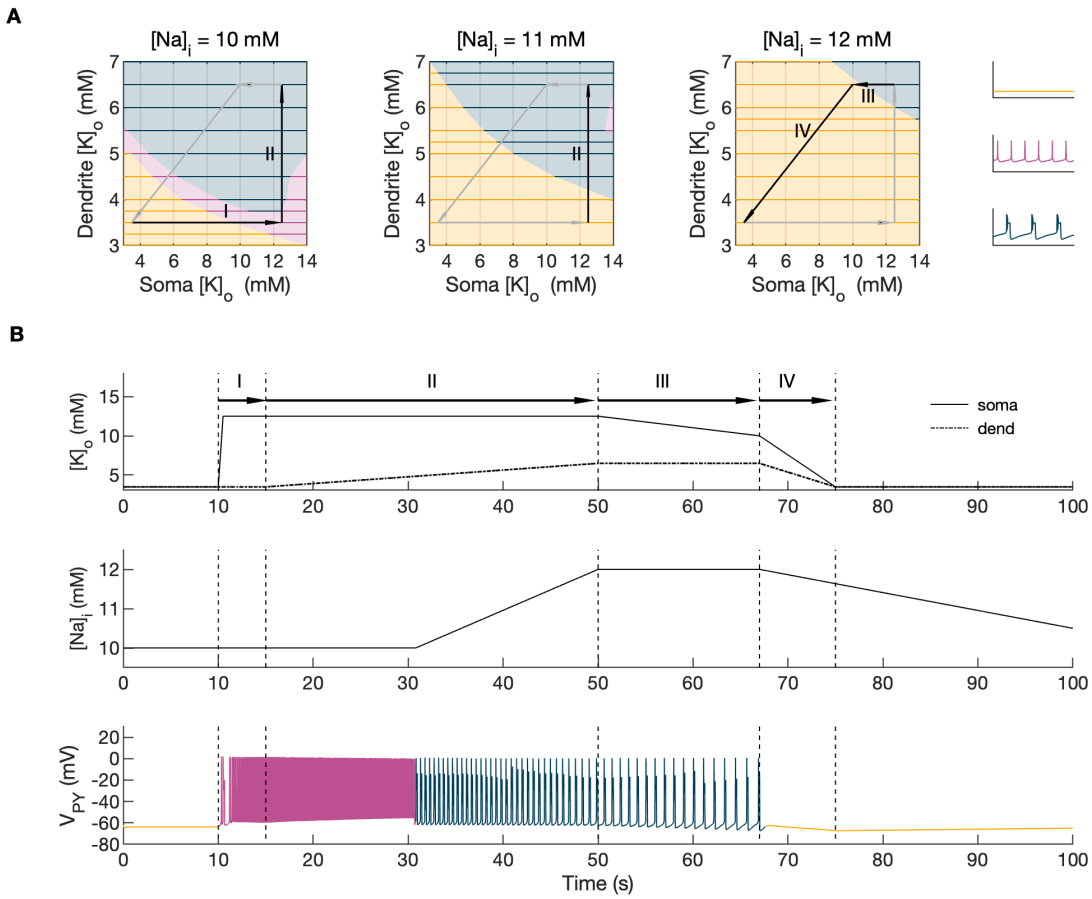

Figure 4. A bifurcation diagram of the model. In the bifurcation analysis extracellular potassium and intracellular sodium concentrations in the PY and IN cells were control parameters. Concentrations of all other ions were fixed at their reference values (except chloride: $[Cl^-]_{i,dend}$ = 7.5 mM), all ion accumulation mechanisms were blocked and background input was removed. **(A)** Bifurcation diagrams showing the dependence of the behavior of the model on

$[K^+]_{o,dend}$ and $[K^+]_{o,soma}$ for varying values of $[Na^+]_i$. The diagram colors correspond to types of activity shown on the right: rest (yellow), tonic firing (violet) and bursting (dark blue). An increase in [Na+]I progressively decreased the domains of tonic firing and bursting and increased the resting domain indicating a general decrease in network excitability. The black and gray arrows correspond to the evolution of $[K^+]_{o,soma}$, $[K^+]_{o,dend}$ during different phases of the SLE, shown in part **B**. **(B)** A simulation of the model with $[K^+]_{o,soma}$, $[K^+]_{o,dend}$ and $[Na^+]_i$ as the external control parameters, that illustrated the occurrence of transitions between different types of activity during the SLE. The top two panels show the time course of $[K^+]_{o,soma}$, $[K^+]_{o,dend}$ and $[Na^+]_i$ and approximate their evolution during the SLE (Fig. 2). The third panel shows the resulting PY cell behavior. The parameter evolution is divided into four phases indicated by the arrows denoted as I–IV in part **A** and **B**. Phase I corresponds to a sharp increase in $[K^+]_{o,soma}$ which led to a transition from rest to tonic firing (marked as a black arrow 'I' in the first panel in **A**). Phase II corresponds to a slow increase in $[K^+]_{o,dend}$ which led to a transition from tonic firing to bursting (marked as a black arrow 'II' in the first and second panels in **A**). Phase III represents a period of increased $[Na^+]_i$ and decreasing $[K^+]_{o,soma}$ which led to the termination of the SLE (represented by a black arrow 'III' with its tip in the yellow domain in the third panel in **A**). Phase IV corresponds to the postictal period with elevated $[Na^+]_i$ and a return of $[K^+]_{o,soma}$, $[K^+]_{o,dend}$ to their baseline values (marked as a black arrow 'IV' in the third panel in **A**).

The role of $[Cl^-]_i$

Chloride accumulation depends on Cl^- currents, but it is also affected by variations in potassium concentrations mediated via KCC2 cotransport. Hence, chloride and potassium could not be considered as independent control parameters in the fast-slow system analysis approach. Furthermore, visualization of the results with four control parameters ($[K^+]_{o,soma}$, $[K^+]_{o,dend}$, $[Na^+]_i$ and $[Cl^-]_i$) is challenging. Therefore, to evaluate the role of chloride accumulation, we compared the reference model with the model in which chloride dynamics was excluded (Fig. 5). In these simulations, afferent excitatory input was removed from the PY cells to eliminate the stochastic component from the analysis. When considering the role of chloride homeostasis mediated via KCC2, the direction of K–Cl cotransport depends on the ratio $[K^+]_i[Cl^-]_i/[K^+]_o[Cl^-]_o$.(J. A. Payne et al., 2003) If $[Cl^-]_i$ is greater than $[K^+]_o$ (disregarding the changes in $[K^+]_i$ and $[Cl^-]_o$, which are relatively small), the ratio is greater than 1 and KCC2 extrudes Cl^- and K^+. If $[K^+]_o$ is greater than $[Cl^-]_i$, the KCC2 flow is reversed and Cl^- and K^+ ions are transported into the cell. When chloride accumulation was removed (Fig. 5A), the reversal potentials of the Cl^- and GABAa

currents (E_{Cl} and E_{GABAa}) were fixed (blue and violet lines in Fig. 5A, second panel). Under such conditions, the firing of the interneuron (Fig. 5A, third panel) exerted a steady inhibitory influence on the PY cells. Additionally, it increased $[K^+]_o$ above fixed $[Cl^-]_i$ level (Fig. 5A, fourth panel). As a result, the KCC2 transported K^+ and Cl^- into the cells (Fig. 5A, bottom panel) and reduced the external K^+ concentration. All these effects prevented the PY cells from firing and the SLE was not manifested, as seen in the LFP signal which displayed only low amplitude fast activity (Fig. 5A, top panel) mediated by GABAa inhibitory postsynaptic currents (IPSC). Conversely, activation of the IN in the reference model, with chloride accumulation intact, led to a typical SLE (Fig. 5B, top panel). The chloride dynamics increased the excitability in three ways: i) it increased the chloride reversal potential (blue line in Fig. 5B, second panel) toward the PY membrane potential and reduced the hyperpolarizing chloride leak current; ii) it increased the GABAa reversal potential that approached the PY cell membrane potential (violet line in Fig. 5B, second panel), reducing the postsynaptic inhibitory current and iii) it contributed to $[K^+]_o$ accumulation as increased $[Cl^-]_i$ reduced the inflow of Cl^- and K^+ into the cell via KCC2 (Fig. 5B, bottom panel).

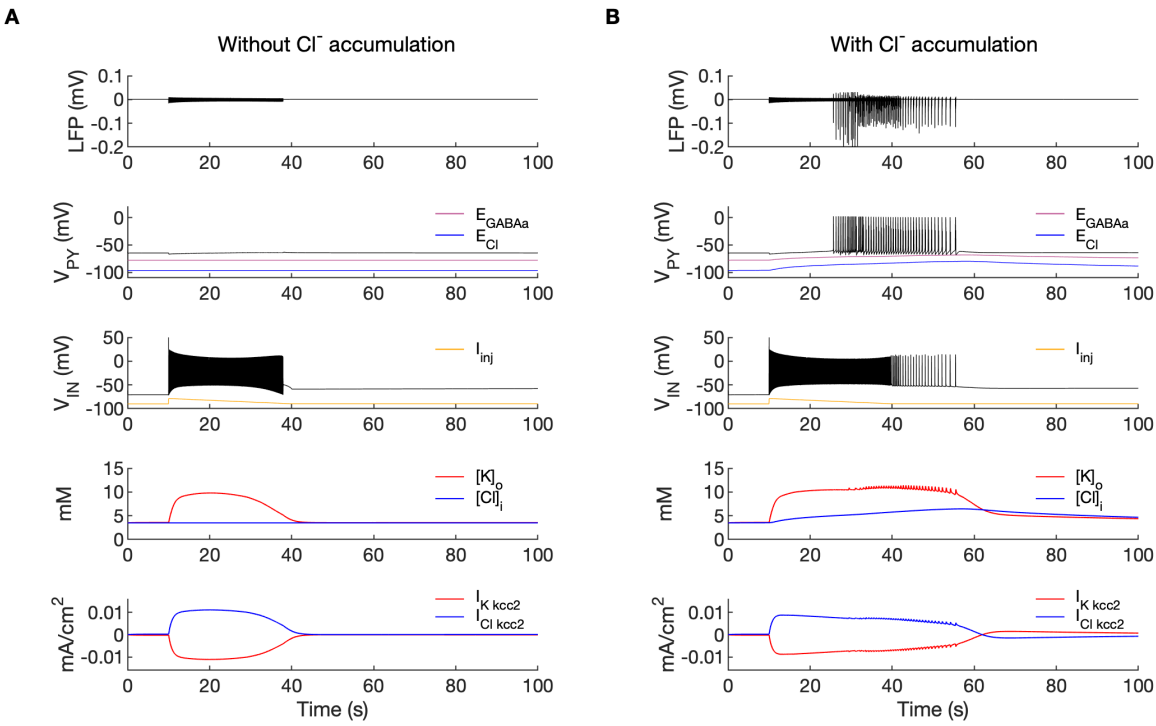

Figure 5. A comparison of the model without and with chloride accumulation. The five panels in each column show (from top to bottom): the LFP signal, the PY cell membrane potential, the IN membrane potential, the extracellular potassium concentration and intracellular chloride concentration combined with the chloride and potassium KCC2 currents in the somatic

299 compartments, respectively. Additionally, the equilibrium potential of chloride and GABAa are
300 shown in the second panel from the top. In **A** and **B**, the background input was removed to
301 exclude the stochastic component. **(A)** When the $[Cl^-]_i$ accumulation mechanism was blocked,
302 the chloride concentration was fixed at the reference value (fourth panel). Without chloride
303 accumulation, the PY cell remained inhibited (second panel) by the IN discharge triggered by
304 the current injection (yellow, third panel). Additionally, elevated $[K^+]_o$ and fixed $[Cl^-]_i$ promoted
305 K^+ influx via KCC2 (bottom panel, red), thus lowering $[K^+]_o$ and further preventing the
306 generation of the SLE. **(B)** With chloride accumulation, the IN discharge led to an increase in
307 E_{Cl} and E_{GABAa} (second panel, blue and violet) which reduced the hyperpolarizing $I_{Cl,leak}$ and
308 I_{GABAa} currents and enhanced excitability. The increased $[Cl^-]_i$ reduced K^+ influx via KCC2
309 (bottom panel, red) which led to prolonged $[K^+]_o$ accumulation (fourth panel, red). All three
310 effects contributed to the SLE.

311 **Model predictions**

312 The computer model generated predictions about features that were not explicitly implemented
313 but were consequences of the elementary neurobiological mechanisms used to create the model.
314 These phenomena are described below. The experimental confirmation of features predicted by
315 a model is an essential step in model validation.

316 *The evolution of the inter-burst interval duration*

317 It is well known that muscle jerking during the clonic phase of tonic-clonic seizure slows down
318 before ceasing when seizure ends (Bromfield et al., 2006). Frequency slowing has also been
319 observed in video sequences (Kalitzin et al., 2016) and electrographic counterparts of a seizure
320 revealed by either EEG (Franaszczuk et al., 1998; Schiff et al., 2000) or EMG (Conradsen et al.,
321 2013). In the model, a gradual increase in the interval between ictal bursts (IBI) was visible (Fig.
322 2A and 3B). To observe the evolution of the IBI more precisely, the background noise was
323 removed from the simulation and was compensated with a steady depolarizing current of 6 pA
324 injected into the somas of all PY cells to preserve the duration of the SLE. A simulated SLE
325 trace and the detected ictal bursts (short bars) are shown in Fig. 6A (top panel). The evolution of
326 the IBI is shown below with either a linear (Fig. 6A, middle panel) or logarithmic (Fig. 6A,
327 bottom panel) y-axis. The IBI on the semi-log graph laid on a straight line suggesting an
328 exponential relationship. The evolution of the IBI during an SLE in a whole-brain *in vitro*
329 preparation (Fig. 6B) and a human TLE seizure (Fig. 6C) exhibited the same characteristics. An

exponential relationship was confirmed via the root mean square error (RMSE) calculated for linear and exponential fits. In all examples, the exponential fit had a lower RMSE.

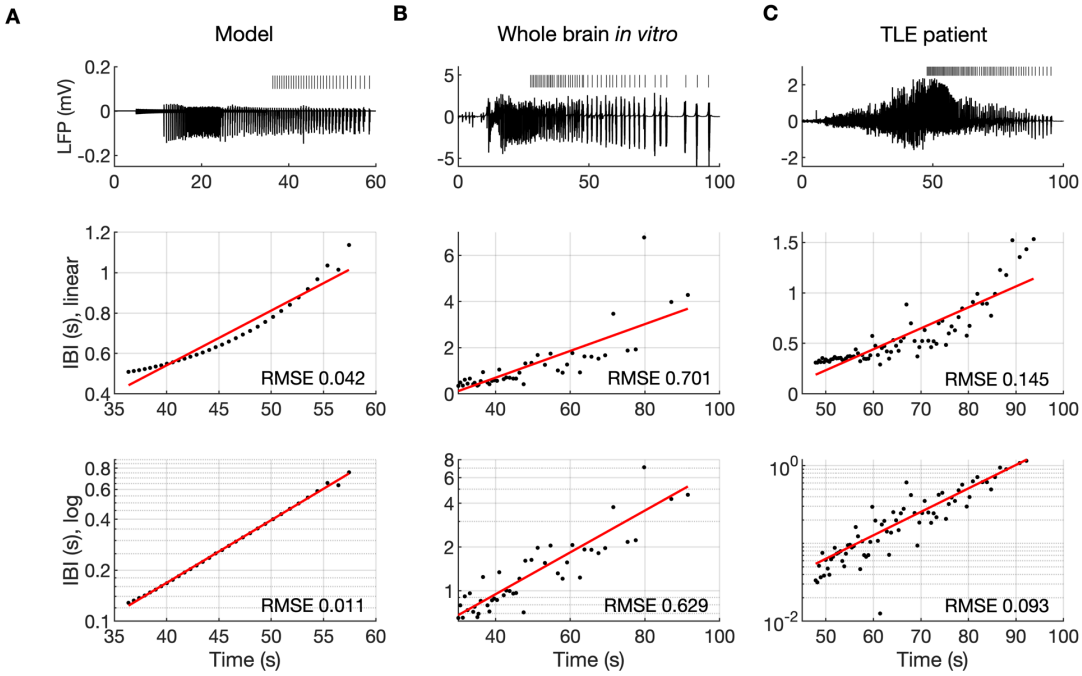

Figure 6. The evolution of IBI in the model and experimental data. (A) In the simulation, the background input was removed and compensated with a small depolarizing current injected into the PY cells to preserve the duration of the SLE. A decreasing rate of bursting is visible in the LPF signal and in the detected bursts marked above the trace (top panel). The evolution of the IBI is shown with the y-axis on a linear scale (middle panel) and a log scale (bottom). On a linear y-axis plot, the data appear curved while on a semi-log plot they lay on a straight line, suggesting exponential scaling of the IBI with time. The red line in each plot represents the best fit for the detected IBI; linear function (middle panel) and exponential function providing a linear relationship on a semi-log plot (bottom panel). The root mean square error (RMSE) between the data points and fitted function is shown in each window. The exponential function fit yielded a smaller RMSE compared to the linear fit, providing quantitative confirmation that at the end of the simulated SLE, the IBI duration increased exponentially, rather than linearly, with time. **(B)** The evolution of the IBI during the SLE induced by application of bicuculline in the whole-brain *in vitro* preparation (Boido et al., 2014; Gnatkovsky et al., 2008). **(C)** IBI evolution during a seizure recorded with intracerebral electrodes positioned in the temporal lobe in a patient submitted to presurgical evaluation (courtesy of Laura Tassi, Epilepsy Surgery Center, Niguarda Hospital, Milano, Italy). In **B** and **C**, the detected IBI lay on a straight line on the semi-log plot

350 and the exponential fit resulted in a smaller RMSE compared to the linear fit, validating the
351 model prediction of an exponential increase in the IBI at the end of a seizure. The linear fit, $IBI(t) = A + Bt$, was obtained using the *polyfit* procedure, while the exponential function, $IBI(t) = A+Bexp(Ct)$, was fitted using the *fminsearch* procedure in Matlab.

354 *The postictal period*

355 An additional model prediction concerned the postictal period which is characterized by reduced
356 excitability and firing. As shown in Fig. 2A–C, after the termination of a seizure there was an
357 approximate 30- to 50-second period during which firing was either absent or reduced with
358 respect to the interictal period. The exact duration of the postictal period was difficult to assess,
359 as the gap in firing after the SLE was dependent on background fluctuations. To directly
360 investigate the network excitability, we analyzed the responsiveness of the model to external
361 periodic stimulation (see Boido et al. (2014)). The background noise was removed and was
362 compensated with a steady depolarizing current, as in Fig. 6. Stimulation was delivered by
363 activating the excitatory synapses every 5 seconds at each PY soma (arrows in Fig. 7B). The
364 amplitude of the excitatory postsynaptic current (EPSC) was set at just above the threshold for
365 triggering the spike in the interictal period (before the timestamp at 60 seconds). The external
366 stimulation triggered two burst responses after the SLE termination (Fig. 7, vertical broke line)
367 and failed to trigger a suprathreshold response for approximately 40 seconds afterwards. In line
368 with the PY response pattern, no response to the simulated stimulation was observed in the LFP
369 signal during the postictal suppression period (Fig. 7A). The high excitability immediately after
370 termination of the SLE (timestamps between seconds 110 and 120) was correlated with elevated
371 $[K^+]_o$ which was present shortly after the SLE (Fig. 7C). The subsequent postictal reduction of
372 excitability was associated with decay of $[K^+]_o$ and an increased hyperpolarizing Na^+/K^+-pump
373 current that decayed with a slower time constant associated with a gradual clearance of $[Na^+]_i$ by
374 the pump (Fig. 7D).

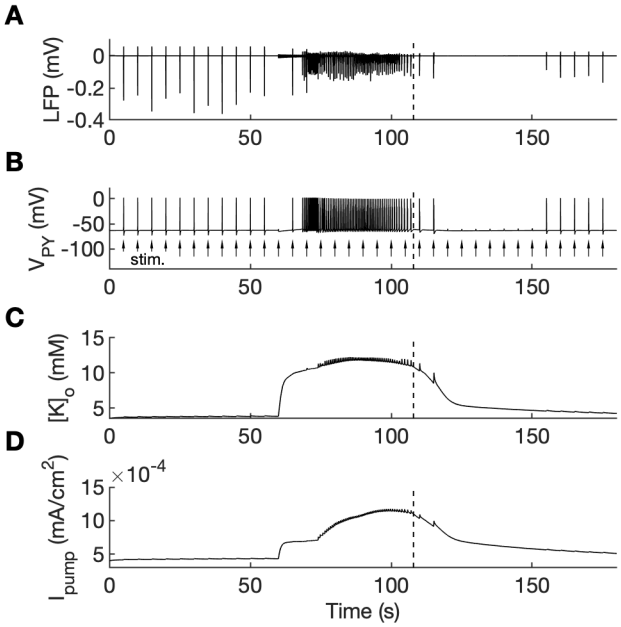

Figure 7. An analysis of network excitability in the postictal period. In this figure, the background input was removed from the simulation and compensated with a small depolarizing current injected into the PY cells, as in Fig. 6. **(A)** The LFP signal. **(B)** The PY cell membrane potential with external periodic stimulation delivered every 5 seconds, marked by the arrows. The amplitude of the stimulation was set at just above the threshold for triggering a spike in the interictal period. **(C)** The extracellular potassium in the somatic compartment. **(D)** The net Na^+/K^+-pump current in the somatic compartment. The vertical broken line in all panels marks the SLE offset time without periodic stimulation. Immediately after termination of the SLE, the network was still excitable due to increased $[K^+]_o$. Shortly afterward, the excitability decreased due to an increased Na^+/K^+-pump current that outlasted the increase in $[K^+]_o$. Increased I_{pump} and decreased $[K^+]_o$ which occurred shortly after the termination of the SLE, led to a postictal period during which the network did not respond to external stimulation for approximately 40 seconds.

Discussion

The present study aimed to better define the mechanisms underlying focal seizures. The ictal pattern most frequently observed in human and experimental TLE, i.e., the LVF onset pattern, exhibits a stereotypical sequence of fast activity, irregular spiking and periodic bursting (as shown in Fig. 3A, first panel) (Avoli et al., 2016; de Curtis & Avoli, 2016; Devinsky et al., 2018; Velascol et al., 2000). We successfully reproduced this pattern in the computer model by

transiently increasing the firing of the IN. After this trigger, the simulated SLE phases evolved autonomously. Our study suggests that various seizure phases and transitions from one phase to another are mediated by feedback mechanisms between neuronal activities, ion concentration changes and ion homeostasis processes. The distinct mechanisms that shape the activities at various seizure stages are discussed below.

Seizure initiation

There is increasing evidence showing that seizures with LVF onset are initiated by discharges of fast-spiking GABAergic interneurons (de Curtis & Avoli, 2016; de Curtis & Gnatkovsky, 2009; Devinsky et al., 2018). Intracellular chloride accumulation and the elevation of $[K^+]_o$ due to interneuron activity leads to subsequent depolarization of PY cells and seizure development. Increased interneuron discharges and decreased PY activity around the time of seizure onset were first evidenced in *in vitro* and *in vivo* animal models (Gnatkovsky et al., 2008; Grasse et al., 2013; Lévesque et al., 2016; Lopantsev & Avoli, 1998; Miri et al., 2018; Toyoda et al., 2015; Ziburkus et al., 2006). A similar scenario was observed with single-unit recordings performed during intracerebral presurgical monitoring in neocortical and temporal lobe epilepsy patients (Elahian et al., 2018; Truccolo et al., 2011). The hypothesis that seizure initiation is related to an elevation in $[K^+]_o$ caused by a strong initial discharge has been tested in computational models with ion concentration changes. In these simulations, seizure-like activity has been induced by DC stimulation of the PY cells alone (Bazhenov et al., 2004; Buchin et al., 2016; Kager et al., 2002), by a brief increase in $[K^+]_o$ (Fröhlich et al., 2006), by stimulation of the IN and PY cells (Ho & Truccolo, 2016) or by varying the extracellular concentration of K^+ and O_2.(Wei et al., 2014) The initial *in silico* tests on seizure initiation by selective involvement of fast-spiking interneurons were conducted earlier by us (Gentiletti et al., 2017) and others (González et al., 2018). We demonstrated that an increase in interneuron firing triggered a transition to a self-sustained SLE. González et al. (2018) showed that interneuron stimulation by current pulses led to the development of an SLE via a gradual increase in $[K^+]_o$ mediated by Cl^--dependent activation of the KCC2 cotransporter. In our present model, the IN was activated by a depolarizing, decreasing current ramp of 30 seconds. Initially, the IN discharge led to the silencing of the PY cells, which was correlated with low amplitude fast activity in the LFP signal. The sustained interneuron activity caused a gradual increase in $[Cl^-]_i$ and $[K^+]_o$ in the PY cells. The increase in $[K^+]_o$ produced a positive shift in the K^+ reversal potential which led to a reduction in the K^+ leak current and membrane depolarization. The accumulation of $[Cl^-]_i$

426 increased the Cl^- reversal potential and decreased the driving force of the Cl^- ions, which led to
427 a reduction in GABAa IPSC and the Cl^- leak current. A depolarization in the E_K, E_{Cl} and E_{GABAa},
428 and a weakening of the associated hyperpolarizing currents resulted in a gradual depolarization
429 of the PY cells and sustained firing, which was correlated with the tonic SLE phase.

430 To address the role of potassium and chloride accumulation in seizure initiation, we
431 considered the elevation of $[K^+]_o$ and $[Cl^-]_i$ separately. As shown in Fig. 5, a selective increase
432 in $[K^+]_o$ with a fixed concentration of Cl^- did not trigger an SLE. The same result was observed
433 when $[Cl^-]_i$ was increased and the concentration of $[K^+]_{o,i}$ remained fixed (not shown). This
434 suggests that in our model, a change in the concentrations of either $[K^+]_o$ or $[Cl^-]_i$ was not
435 sufficient to initiate an SLE and that an increase in both is necessary. These findings corroborate
436 the results of a study by Alfonsa et al. (2015) which demonstrated that optogenetic chloride
437 loading of PY cells did not trigger ictal events, while the addition of a subictal dose of 4-
438 aminopyridine (4-AP) led to full ictal activity.

439 The observation that the development of seizures may be related to an increase in $[K^+]_o$
440 beyond the physiological values suggests that the modulation of $[K^+]_o$ by the use of K^+ chelators
441 is a potential strategy for the control of seizures. Moreover, in our previous work, we
442 demonstrated that an artificial potassium buffer, which mimicked the function of astrocytes by
443 balancing neuronal K^+ release, could reduce neuronal excitability and prevent an SLE
444 (Suffczynski et al., 2017).

445 **The mechanisms of $[K^+]_o$ accumulation**

446 A question arises: what causes $[K^+]_o$ accumulation? The buildup of Cl^- inside the PY neurons
447 during interneuron-induced GABA release results in the activation of the KCC2 cotransporter,
448 which extrudes Cl^- and K^+ into the extracellular space. This hypothesis is supported by *in vitro*
449 experiments which showed that activation of GABAa receptors led to an increase in $[K^+]_o$ and
450 cell depolarization, which were eliminated by the KCC2 inhibitor, furosemide (Viitanen et al.,
451 2010). The above-mentioned hypothesis is also consistent with the findings that the application
452 of the KCC2 blockers VU0240551 and bumetanide prevented SLEs during 4-AP application in
453 rat brain slices (Hamidi & Avoli, 2015). However, it is not clear whether the ictal activity is
454 consistently based on K^+ efflux through KCC2. In the pilocarpine model, the enhancement of
455 KCC2 in principal cortical neurons is associated with a reduction in seizure duration (Magloire
456 et al., 2019). Based on these results, the authors suggested that KCC2 activity does not affect

seizure initiation, but influences seizure maintenance during a prolonged period of Cl^- accumulation. The antiepileptic role of enhanced KCC2 activity has also been suggested by Moore et al. (2018), who showed that KCC2 potentiation delayed the onset of an SLE after 4-AP application *in vitro* and reduced the severity of kainate-induced seizures *in vivo*. When considering the role of KCC2 in $[K^+]_o$ accumulation, it is necessary to note that the direction and magnitude of KCC2 transport depend on the concentration gradients of Cl^- and K^+ (Kaila et al., 2014). Under normal conditions, when $[K^+]_o$ is sufficiently controlled by homeostatic mechanisms, GABAergic activity leads to the extrusion of Cl^- and K^+. However, an increase in $[K^+]_o$ may reverse the K^+–Cl^- cotransport, thus contributing to $[K^+]_o$ buffering rather than accumulation (Payne, 1997; Thompson & Gahwiler, 1989) The activation of IN in our model led to a rapid increase in K^+ in the narrow extracellular interstitial compartments, while intracellular Cl^- accumulation was more gradual (Fig. 2). This generated an influx of K^+ and Cl^- via KCC2 (Fig. 5B), which led to $[K^+]_o$ buffering and $[Cl^-]_i$ accumulation. The exclusion of KCC2 involvement in the increase in $[K^+]_o$ suggests that the primary mechanism of $[K^+]_o$ accumulation in our model was due to other processes, such as the outward K^+ current that repolarizes action potentials in activated IN and PY cells. This observation is consistent with *in vivo* experimental evidence that showed a significant local $[K^+]_o$ rise due to increased spiking activity following electrical stimulation of the cat cerebral cortex (Heinemann & Lux, 1975).

The tonic-to-bursting transition

Potassium ions released by interneuron discharges initially diffused to the somatic extracellular compartments of the PY cells and contributed to PY soma depolarization and tonic firing, as described above. Subsequently, K^+ diffusion from the somatic to dendritic compartments promoted regenerative dendritic spikes in PY cells (Fig. 2D). High $[K^+]_o$ in the soma and dendrites favored burst firing (Supplementary Fig. S1) through the reduction of repolarizing K^+ currents, the activation of a Na^+ persistent current, and a shift from spike after-hyperpolarization toward depolarizing after-potentials. Prolonged depolarization led to the activation of slow M-type K^+ conductance (Supplementary Fig. S2), which hyperpolarized the PY cells after a series of fast spikes. The bursting mechanism in our model originated from currents used in the original entorhinal cortex cells model (Fransen et al., 2002) and was similar to the mechanism in CA1 neurons (Golomb et al., 2006).

488 **Seizure termination**

489 Various mechanisms underlying seizure termination have been suggested (Lado & Moshé, 2008;
490 Zubler et al., 2014), however, researchers have not yet reached a consensus regarding which one
491 plays a dominant role. In our model, the SLE terminated spontaneously. Following the fast-slow
492 analysis approach (Fröhlich et al., 2006) we created a simplified model in which $[K^+]_{o,soma}$,
493 $[K^+]_{o,dend}$ and $[Na^+]_i$ were treated as control parameters. Hence, the influence of neuronal activity
494 on ionic variations was removed and the dependence of network activity on K^+ and Na^+
495 concentrations was analyzed (Fig. 4A). When the time course of the concentration changes of
496 these two ions were tuned to reproduce the decrease in $[K^+]_o$ and increased level of $[Na^+]_i$
497 observed in the late SLE phase, the ictal activity spontaneously terminated (Fig. 4B). This
498 indicates that SLE cessation in the model can be explained by two coincident factors, namely
499 the decrease in $[K^+]_o$ during stable levels of increased $[Na^+]_i$. An increase in $[Na^+]_i$ led to an
500 increased hyperpolarizing Na^+/K^+-pump current, which increased the firing threshold in the
501 neurons. The increased pump activity also contributed to a progressive decrease in $[K^+]_o$.
502 Potassium repolarization currents increased after each burst and eventually prevented the
503 initiation of a new cycle of the oscillation. The idea that negative feedback between $[Na^+]_i$
504 accumulation and neuronal firing is responsible for seizure termination was first formulated by
505 Jensen & Yaari (1997). Even though it has not been tested experimentally, this hypothesis is
506 consistent with the observation that the inhibition of Na^+/K^+-pump activity occurring during
507 hypoxia prolongs SLE discharges in hippocampal slices with blocked synaptic transmission
508 (Haas & Jefferys, 1984). It was also observed that a decrease in Na^+ channel conductance via the
509 antiepileptic drug phenytoin, increased the seizure threshold but prolonged the afterdischarges
510 and seizure durations in the rat kindling model of epilepsy (Ebert et al., 1997). In the
511 computational model developed by the Bazhenov team (Krishnan et al., 2015; Krishnan &
512 Bazhenov, 2011) and Chizhov et al. (2018), a progressive increase in $[Na^+]_i$ and activation of the
513 electrogenic Na^+/K^+-pump were identified as the primary factor of SLE termination. The seizure
514 termination mechanism in the above-mentioned studies is similar to the mechanism observed in
515 the present study, even though different specifications of neuronal mechanisms, network
516 characteristics and seizure morphologies were used.

517 It should be also noted that activation of the Na^+/K^+-pump by $[Na^+]_i$ is not the only
518 proposed mechanism of seizure termination. An alternative mechanism, also linked to an
519 increase in $[Na^+]_i$, is dependent on the Na^+-activated K^+ channels (Igelström, 2013). Moreover,

many other mechanisms such as acidosis (Ziemann et al., 2008), the upregulation of inhibitory neurons (Wen et al., 2015), glutamate depletion (Lado & Moshé, 2008), the depolarization block of neurons mediated by K^+ release from astrocytes (Bragin et al., 1997), after-hyperpolarization due to K^+ channels (Timofeev & Steriade, 2004), postburst depression (Boido et al., 2014), increased synchrony (Schindler et al., 2007) and the release of adenosine (During & Spencer, 1992; Uva & de Curtis, 2020) have been suggested to play a role in seizure termination. The abrupt termination of a seizure across the entire brain requires long-range communication which may involve thalamocortical interactions (Aracri et al., 2018; Evangelista et al., 2015), travelling waves (Martinet et al., 2017; Proix et al., 2018) and ephaptic interactions (Jefferys, 1995; Shivacharan et al., 2019). Multiple neuromodulatory, ionic, synaptic and neuronal components likely cooperate to terminate a seizure. Further insight into these mechanisms may be obtained by their selective blockage (Uva & de Curtis, 2020), the tracking of EEG signal changes as seizure offset approaches (Boido et al., 2014; Saggio et al., 2020) and from analysis of the duration of postictal suppression (Payne et al., 2018).

Frequency Slowing

The approach of seizure termination is often (but not always) accompanied by an increase in the intervals between successive bursts that form the late seizure phase. Saggio et al. (2020) analyzed frequency slowing in human focal onset seizures and estimated that approximately 40% exhibited unequivocal discharge slowing down toward the end. Burst frequency slowing was confirmed in a study on the entorhinal cortex of the isolated brain preparation during bicuculline- and 4AP-induced SLE (Boido et al., 2014). Our model prediction of the exponential increase in the IBI toward the SLE offset (Fig. 6A) was confirmed with experimental data (Fig. 6BC). These findings are also consistent with those of Bauer et al. (2017), which demonstrated that inter-burst intervals in focal epilepsy patients were predominantly described by the exponential scaling law. Conversely, it has been suggested that depending on the bifurcation which leads to seizure termination, the burst oscillation frequency can be constant or decrease according to the logarithmic or square root relationship (Jirsa et al., 2014). The IBI scaling law depends on the slow process leading to seizure termination. In our model, termination of the seizure was related to the slow evolution of ion concentrations which led to a progressive decrease in excitability, primarily via an increased Na^+/K^+-pump rate. The lower the excitability, the more time it took for the burst firing threshold to be reached. Hence, bursts frequency slowing in the model was causally related to variations in ion concentrations. If the time course of the ionic concentrations

were different, the evolution of the IBI would also shift. Several alternative explanations for the increasing inter-burst intervals have been proposed. Bauer et al. (2017) included a plasticity parameter that progressively decoupled spatially distributed neural mass units based on the synchrony level. This mechanism accounted for seizure termination, exponential IBI increase and the presence of a transient postictal state. In the model of Liou et al. (2020) the IBI was constant during seizure expansion and only when the spatial propagation of ictal discharge ceased, the seizure entered the pre-termination stage with a slowing-down trend. An increase in the IBI in this phase was related to the recovery of inhibition and restoration of the Cl^- concentration gradient. These studies indicate that spatial properties related to seizure propagation and synchrony are other factors that may affect the evolution of the IBI.

The postictal period

Seizures are followed by the suppression of physiological rhythms known as postictal EEG suppression (PES) that lasts for seconds or minutes (Pottkämper et al., 2020). Using the stimulation protocol, we investigated the duration of PES in the model. Our results showed that shortly after termination of the SLE, burst responses were still triggered, however, after few seconds, the excitability decreased and remained reduced for approximately 40 seconds (Fig. 7B). This postictal reduction in excitability was associated with subsequent decay of $[K^+]_o$ and an increased hyperpolarizing Na^+/K^+-pump current, which decreased gradually due to slow clearance of $[Na^+]_i$ by the pump (Fig. 7D). The PES duration in our model is consistent with single-unit recordings in epileptic patients that are suppressed for 5 to 30 seconds after seizure termination (Truccolo et al., 2011). Our *in silico*-derived prediction that postictal 'silence' depends on the hyperpolarizing Na^+/K^+-pump has been previously suggested (Fisher & Schachter, 2000) and simulated (Krishnan et al., 2015; Krishnan & Bazhenov, 2011). However, in these models, an increased Na^+/K^+-pump rate due to elevated $[Na^+]_i$ terminated the SLE and reduced $[K^+]_o$ to below baseline level, resulting in a postictal state via a negative shift in E_K and membrane hyperpolarization. A below-reference value of $[K^+]_o$ was observed after seizure termination (Heinemann et al., 1977) and may lead to decreased excitability. In our model, the postictal state was not associated with $[K^+]_o$ undershoot, as it decayed to baseline level within a few seconds after the SLE offset (Fig. 7C). This was also observed in several previous studies (Fisher et al., 1976; Futamachi et al., 1974). The findings generated by our computational model suggest that the mechanisms of seizure termination and PES involve ion homeostatic processes

activated and sustained by the excessive seizure discharges, eventually leading to the cessation of the seizure and restoration of the normal state.

Methods

Geometry

The cell morphology was based on entorhinal cortex PY cells and an interneuron model (Fransen et al., 2002), further reduced to equivalent cylinder models. The PY consisted of two compartments: a soma with a length of 20 μm and a diameter of 15 μm, and a dendrite with a length of 450 μm and a diameter of 6.88 μm. The interneuron only had a somatic compartment with a length of 20 μm and a diameter of 15 μm. Each compartment was surrounded by its own extracellular space (ECS). The extracellular compartments were embedded in a common bathing medium which represented the surrounding neural tissue and vasculature. The size of the ECS was estimated by the extracellular volume fraction, α defined as the ratio volume of extracellular space/volume of tissue. We used $\alpha = 0.131$ which corresponded to the CA1 *st. pyramidale* and a K^+ concentration of 3.5 mM (McBain et al., 1990).

Biophysics

The active membrane currents in the PY were the fast Na^+ and K^+ currents (I_{Na} and I_{Kdr}, respectively) in both compartments and were responsible for action potential generation; a persistent Na^+ current, I_{NaP} in the soma; a high-threshold Ca^{2+} current, I_{CaL} in both compartments; a calcium-dependent after-hyperpolarization K^+ current, I_{KAHP} in both compartments; a fast calcium- and voltage-dependent K^+ current, I_{KC} in both compartments; and a noninactivating muscarinic K^+ current, I_{KM} in the soma. The IN included only the I_{Na} and I_{Kdr} currents responsible for spike generation. All the equations for the active currents were initially based on those described by Fransen et al. (2002), however, an additional modification of the parameters described below was required to account for ionic regulation mechanisms. Simulations were performed using the NEURON simulator with a fixed integration step of 0.05 ms.

Passive properties

The reversal potentials were obtained via the Nernst equation:

$$E_X = 2.3\frac{RT}{zF}\log\left(\frac{[X]_o}{[X]_i}\right)$$

where $[X]_i$ and $[X]_o$ are intra- and extracellular concentrations, respectively, of the ions. X = {Na^+, K^+, Ca^{2+}, Cl^-}, F is the Faraday constant, R is the gas constant, z is the valence of the ions and T = 273,16 + 32 is the absolute temperature (Gnatkovsky et al., 2008). A leak current, I_{leak}, was present in all compartments of both cells and was a sum of the leak currents of Na^+, K^+ and Cl^-, modelled as:

$$I_{i,leak} = g_{i,leak}(V - E_i)$$

where $g_{i,leak}$ is the leak current conductance of the ion of interest i = {Na^+, K^+, Cl^-}. The resting membrane potential was -62 mV in the pyramidal cell and -70 mV in the interneuron. The specific axial resistance in both cells was set to R_a = 100 Ohm*cm and the specific membrane capacitance was set to C_m = 1μF/cm^2, as in Fransen et al. (2002). Based on the R_a and PY cell geometry, the somato-dendritic coupling conductance, g_c, was calculated as 1.5 mS.

Active currents

The original equations used time constant units in seconds (s) and voltage units in volts (V), with 0 V corresponding to the resting membrane potential. All equations were modified to account for the millivolt (mV) and millisecond (ms) units used in our model and the voltage was shifted by -60 mV to correspond to the membrane potential relative to the extracellular space, which was assumed to be 0 mV. Additional modifications of the parameters were required to account for the ionic regulation mechanisms that were not present in the original model. I_{NaP}: the activation gate exponent was 2 and the inactivation gate time constant, τ_h, was estimated by fitting the activation function form described by Fransen et al. (2002) to the experimental data (Magistretti & Alonso, 1999). I_{Kdr}: the steady-state activation function, n_{inf}, and the activation gate time constant, τ_n, were estimated by empirical fit to the experimental data (Sah et al., 1988). To increase the firing threshold, the activation curve was shifted toward positive potentials by 16 mV in the soma and 7 mV in the dendrites. The model generated spontaneous fast spiking otherwise. I_{KAHP}, I_{KC}: these Ca^{2+}-dependent currents were modelled according to the model described by Traub et al. (2003) and were implemented in ModelDB (https://senselab.med.yale.edu/ModelDB/), accession number 20756. Due to the arbitrary units for Ca^{2+} concentration in Traub's model, we modified the current formula to correspond to mM units and resting level of $[Ca^{2+}]_i$ used in our model. In pyramidal cells, the soma and dendrite

membrane potentials, V_s and V_d, respectively, were governed by the following Hodgkin-Huxley equations:

$$C\frac{dV_s}{dt} = -I_{Na,soma} - I_{NaP} - I_{Kdr,soma} - I_{CaL} - I_{KAHP} - I_{KC} - I_{KM} - I_{leak} - I_{NaKpump} - I_{Capump} - g_c(V_s - V_d) - I_{syn}$$

$$C\frac{dV_d}{dt} = -I_{Na,dend} - I_{Kdr,dend} - I_{CaL} - I_{KAHP} - I_{KC} - I_{NaKpump} - I_{CaPump} - g_c(V_d - V_s) - I_{syn}$$

Transient sodium current

$$I_{Na,soma} = g_{Na,PYsoma} m^3 h(V - E_{Na})$$

$$I_{Na,dend} = g_{Na,PYdend} m^2 h(V - E_{Na})$$

Persistent sodium current:

$$I_{NaP} = g_{NaP} m^2 h(V - E_{Na})$$

Delayed rectifier:

$$I_{Kdr,soma} = g_{Kdr,PYsoma} n^4 (V - E_K)$$

$$I_{Kdr,dend} = g_{Kdr,PYdend} n^2 (V - E_K)$$

High-threshold Ca^{2+} current:

$$I_{CaL} = g_{CaL} m^2 (V - E_{Ca})$$

Ca^{2+}-dependent K^+ (afterhyperpolarization) current:

$$I_{KAHP} = g_{KAHP} m(V - E_K)$$

Fast Ca^{2+}- and voltage-dependent K^+ current

$$I_{KC} = g_{KC} \min([Ca^{2+}]_i/250,1)\, m(V - E_K)$$

Muscarinic current:

$$I_{KM} = g_{KM} m(V - E_K)$$

Equations of gating variables are given in Table 1. Conductance values are given in Table 2.

Table 1. Gating variables of the ionic currents in pyramidal cell model

Current	Kinetics/time constant (ms)	
$I_{Na,soma}$	$\alpha_m = \frac{0.8(-V-40.8)}{\exp\left(\frac{-V-40.8}{4}\right)-1}$	$\beta_m = \frac{0.7(V-15.8)}{\exp\left(\frac{V-15.8}{5}\right)-1}$
	$\alpha_h = 0.32\exp\left(\frac{-V-18}{18}\right)$	$\beta_h = \frac{10}{\exp\left(\frac{-V-18}{5}\right)+1}$
$I_{Na,dendrite}$	$\alpha_m = \frac{0.32(-V-50.9)}{\exp\left(\frac{-V-50.9}{4}\right)-1}$	$\beta_m = \frac{0.28(V-15.9)}{\exp\left(\frac{V-15.9}{5}\right)-1}$

	$\alpha_h = 0.128\exp\left(\frac{-V-45}{18}\right)$	$\beta_h = \frac{10}{\exp\left(\frac{-V-22}{5}\right)+1}$
I_{NaP}	$m_\infty = \frac{1}{1+\exp\left(\frac{-48.7-V}{4.4}\right)}$	$\tau_m = \frac{1}{\frac{0.091(V+38)}{1-\exp\left(\frac{-V-38}{5}\right)} - \frac{0.062(V+38)}{1-\exp\left(\frac{V+38}{5}\right)}}$
	$h_\infty = \frac{1}{1+\exp\left(\frac{48.8+V}{9.98}\right)}$	if $V_m \leq -60$: $\tau_m = 3700 + \frac{2000}{\frac{0.091(V+60)}{1-\exp\left(\frac{-V-60}{5}\right)} - \frac{0.062(V+60)}{1-\exp\left(\frac{V+60}{5}\right)}}$ if $V_m > -60$: $\tau_m = 1200 + \frac{8000}{\frac{0.091(V+74)}{1-\exp\left(\frac{-V-74}{5}\right)} - \frac{0.062(V+74)}{1-\exp\left(\frac{V+74}{5}\right)}}$
$I_{Kdr,soma}$	$n_\infty = \frac{1}{1+\exp\left(\frac{-20.8-V}{13.6}\right)}$	$\tau_m = \frac{1.6\left(C+\exp\left(\frac{V}{5}\right)\right)}{D\exp\left(-\frac{V}{40}\right)\left(C+\exp\left(\frac{V}{5}\right)\right)+0.016\exp\left(\frac{V}{5}\right)(64.9+V)}$ $C = -0.00000230599;\ D = 0.0338338$
$I_{Kdr,dend}$	$n_\infty = \frac{1}{1+\exp\left(\frac{-11.8-V}{13.6}\right)}$	$\tau_m = \frac{1.6\left(C+exp\left(\frac{V}{5}\right)\right)}{Dexp\left(-\frac{V}{40}\right)\left(C+exp\left(\frac{V}{5}\right)\right)+0.016\,exp\left(\frac{V}{5}\right)(64.9+V)}$ $C = -0.00000230599;\ D = 0.0338338$
I_{CaL}	$\alpha_m = \frac{1.6}{1+exp(-0.072(V-5))}$	$\beta_m = \frac{0.02(V+8.9)}{exp\left(\frac{V+8.9}{5}\right)-1}$
I_{KAHP}	$\alpha_m = 2000([Ca]_i - [Ca]_{i,rest})$	$\beta_m = 0.01$
I_{KC}, if $V_m \leq -10$	$\alpha_m = \frac{exp\left(\frac{V+50}{11} - \frac{V+53.5}{27}\right)}{18.975}$	$\beta_m = 2exp\left(-\frac{V+53.5}{27}\right) - \alpha_m$
I_{KC}, if $V_m > -10$	$\alpha_m = 2exp\left(-\frac{V+53.5}{27}\right)$	$\beta_m = 0$
I_{KM}	$m_\infty = \frac{1}{1+exp\left(-\frac{V+35}{5}\right)}$	$\tau_m = \frac{1000}{3.3\left[exp\left(\frac{V+35}{40}\right)\right]+\left[exp\left(-\frac{V+35}{20}\right)\right]}$

Membrane potential of the interneuron was governed by the following Hodgkin-Huxley equations:

$$C\frac{dV}{dt} = -I_{Na} - I_{Kdr} - I_{leak} - I_{NaKpump} - I_{syn} - I_{stim}$$

Current equations, kinetics and time constants of these currents were the same as in pyramidal cell soma. Due to lower resting membrane potential in the interneuron as compared to pyramidal cell, activation curve of I_{Na} was shifted 2 mV towards more negative potential values, while activation curve of I_{Kdr} was shifted 14 mV towards more negative potential values.

Table2. Conductances used in the model

Current conductance	Description	Values (mS/cm^2)
$g_{Na,leak,PY}$	$I_{Na,leak}$ conductance in PY soma and dendrite	$0.9*10^{-5}$
$g_{K,leak,PY}$	$I_{K,leak}$ conductance in PY soma and dendrite	$2.2*10^{-5}$
$g_{Cl,leak,PY}$	$I_{Cl,leak}$ conductance in PY soma and dendrite	$1*10^{-6}$
$g_{Na,PYsoma}$	I_{Na} conductance in PY soma	0.02
$g_{Na,PYdend}$	I_{Na} conductance in PY dendrite	0.002
$g_{Kdr,PYsoma}$	I_{Kdr} conductance in PY soma	0.03
$g_{Kdr,PYdend}$	I_{Kdr} conductance in PY dendrite	0.0035
g_{NaP}	I_{NaP} conductance in PY soma	$60*10^{-5}$
g_{CaL}	I_{CaL} conductance in PY soma and dendrite	$15*10^{-5}$
g_{KAHP}	I_{KAHP} conductance in PY soma and dendrite	$5*10^{-5}$
g_{KC}	I_{KC} conductance in PY soma and dendrite	0.196*1e3
g_{KM}	I_{KM} conductance in PY soma	0.007
$g_{Na,leak,IN}$	$I_{Na,leak}$ conductance in IN	$0.8*10^{-5}$
$g_{K,leak,IN}$	$I_{K,leak}$ conductance in IN	$2.2*10^{-5}$
$g_{Cl,leak,IN}$	$I_{Cl,leak}$ conductance in IN	$5*10^{-6}$
$g_{Na,IN}$	I_{Na} conductance in IN	0.025
$g_{Kdr,IN}$	I_{Kdr} conductance in IN	0.055

Ionic dynamics

The model included six types of ions (K^+, Na^+, Cl^-, Ca^{2+}, A^- and HCO_3^-) with variable intra- and extracellular concentrations (except for HCO_3^-). The evolution of the ion concentrations was based on the following equations:

$$\frac{d[K^+]_i}{dt} = J_K^i + J_{K,longitudinal}^i + J_{K,KCC2}^i + J_{K,Pump}^i + J_{K,vol}^i$$

$$\frac{d[K^+]_o}{dt} = J_K^o + J_{K,radial} + J_{K,longitudinal}^o + J_{K,bath} + J_{K,KCC2}^o + J_{K,Pump}^o + J_{glia} + J_{K,vol}^o$$

$$\frac{d[Na^+]_i}{dt} = J^i_{Na} + J^i_{Na,longitudinal} + J^i_{Na,Pump} + J^i_{Na,vol}$$

$$\frac{d[Na^+]_o}{dt} = J^o_{Na} + J_{Na,radial} + J^o_{Na,longitudinal} + J_{Na,bath} + J^o_{Na,Pump} + J^o_{Na,vol}$$

$$\frac{d[Cl^-]_i}{dt} = J^i_{Cl} + J^i_{Cl,GABAa} + J^i_{Cl,longitudinal} + J^i_{Cl,KCC2} + J^i_{Cl,vol}$$

$$\frac{d[Cl^-]_o}{dt} = J^o_{Cl} + J^o_{Cl,GABAa} + J^o_{Cl,longitudinal} + J_{Cl,bath} + J^o_{Cl,KCC2} + J^o_{Cl,vol}$$

$$\frac{d[Ca^{2+}]_{i,tot}}{dt} = J^i_{Ca} + J^i_{Ca,longitudinal} + J^i_{CaPump} + J^i_{Ca,vol}$$

$$\frac{d[Ca^+]_o}{dt} = J^o_{Ca} + J^o_{Ca,longitudinal} + J^o_{CaPump} + J^o_{Ca,vol}$$

$$\frac{d[A^-]_i}{dt} = J^i_{A,vol}$$

where $[Ca^{2+}]_{i,tot}$ is the total intracellular calcium concentration (see calcium buffer below). All fluxes (mM/ms) are specified below.

Membrane currents

The contribution of transmembrane currents to variations in intra- and extracellular ion concentrations was obtained via the following equations:

$$J^i_X = -\frac{\sum I_X S}{zFV_i}$$

$$J^o_X = \frac{\sum I_X S}{zFV_o}$$

where the sum of I_X is a net membrane current carrying ion X, S is the surface area of the compartment, z is the valence of the ions, F is the Faraday constant and V_i and V_o are the volumes of the intra- and extracellular compartments.

Longitudinal diffusion.

Longitudinal diffusion of K^+, Na^+, Ca^{2+} and Cl^- was implemented between the somatic and dendritic compartments in the intracellular and extracellular space of the same cell. It was described by Fick's first law:

$$J^{io}_{X,longitudinal} = D_x \frac{([X]_{io,a} - [X]_{io})S}{LV_{io}}$$

where D_x is the diffusion coefficient for the ion X, $[X]_{io}$ is the ion concentration in a given intra- or extracellular compartment, $[X]_{oi,a}$ is the ion concentration in the adjacent compartment, S is

the cross-sectional area between the compartments, V_{io} is the compartment volume, L is the distance between the centers of the compartments. The diffusion coefficients were (in um^2/ms): $D_{Na} = 1.33$, $D_K = 1.96$, $D_{Ca} = 0.6$, $D_{Cl} = 2.03$ (as in Somjen et al., 2008).

Radial diffusion.

Na^+ and K^+ ions diffused radially between adjacent extracellular compartments modeled as concentric shells around the neurons. The radial exchange of ions between adjacent shells was described by Fick's first law:

$$J_{X,radial} = D_x \frac{\sum([X]_{o,a} - [X]_o)S}{drV}$$

where $[X]_o$ is the ion concentration in a given shell and the sum goes over all adjacent shells having concentrations $[X]_{o,a}$, V is a given shell volume, dr is the distance between the centers of the shells and S is the surface contact area between the shells calculated at 16% of the total outer shell surface. The electrostatic drift of ions was neglected as the ion movement due to the electrical potential gradient in the extracellular space was small compared to the diffusion.

Diffusion to/from the bath

Radial diffusion of K^+, Na^+ and Cl^- between the ECS and the bath was described by Fick's first law:

$$J_{X,bath} = \frac{1}{s} D_x \frac{([X]_{bath} - [X]_o)S}{drV}$$

where D_x is the diffusion coefficient for the ion X, s is the scaling constant, S is the outer surface of the shell, $[X]_{bath}$ is the bath concentration of the ion X, $[X]_o$ is the ion concentration in a given shell, V is the shell volume, dr is the distance between the extracellular space and the bath (assumed to be half of the shell thickness). Flux J_{bath} represents various processes such as diffusion to more distant areas of the brain and cerebrospinal fluid, active transport of potassium into capillaries and potassium spatial buffering by astrocytes. The effective time constant of these joint processes is likely to be much slower than that of radial and longitudinal diffusion and is described by the scaling constant $s = 4*10^4$.

The Na^+/K^+ pump

The Na^+/K^+ pump was modelled as the sodium and potassium transmembrane currents (Kager et al., 2000):

$$I_{Na,Pump} = 3I_{max} flux([Na^+]_i, [K^+]_o)$$

$$I_{K,Pump} = -2I_{max} flux([Na^+]_i, [K^+]_o)$$

$$flux([Na^+]_i, [K^+]_o) = \left(1 + \frac{Km_K}{[K^+]_o}\right)^{-2} \left(1 + \frac{Km_{Na}}{[Na^+]_o}\right)^{-3}$$

with I_{max} = 0.008 mA/cm^2, Km_K = 2 mM and Km_{Na} = 10 mM. As in the previous model, ion concentrations and membrane potentials at rest deviated slightly from the equilibrium conditions, with and without background excitatory synaptic input. This was due to the presence of the Na^+/K^+-pump glial buffer and ion diffusion, which cannot be balanced and induce small oscillations around the baseline values.

KCC2 cotransport

The KCC2 cotransporter currents were modelled according to Wei et al. (2014):

$$I_K = \gamma U_{KCC2} \log\left(\frac{[K^+]_i [Cl^-]_i}{[K^+]_o [Cl^-]_o}\right)$$

$$I_{Cl} = -I_K$$

with cotransporter strength, U_{KCC2} = 0.3 mM/s. Conversion factor $\gamma = (FV)/S$ from mM/s units to current density units mA/cm^2 was calculated for soma and dendrites based on the compartment surface area (S), intracellular volume (V_i) and the Faraday constant (F).

Glial uptake

Potassium uptake by the glia was modelled as a set of differential equations (Kager et al., 2000):

$$J_{glia} = -k_2[K^+]_o[B] + k_1[KB]$$

$$\frac{d[B]}{dt} = -k_2[K^+]_o[B] + k_1[KB]$$

$$\frac{d[KB]}{dt} = k_2[K^+]_o[B] - k_1[KB]$$

where *[B]* is the free buffer, *[KB]* is the bound buffer (= $[B]_{max}$–*[B]*), B_{max} = 500 mM. k_1 = 0.0008 ms^{-1} and $k_2 = \frac{k_1}{1+\exp\left(\frac{[K]_o-18}{-1.25}\right)}$ are backward and forward rate constants, respectively.

The calcium pump and buffer

The calcium pump and buffer which altered the intracellular Ca^{2+} were modelled according to the model implementation of Somjen et al. (2008) in ModelDB, accession number 113446. The calcium pump which extruded Ca^{2+} from the cells was modelled as a Ca^{2+} transmembrane current:

$$I_{CaPump} = \frac{I_{max}}{1 + \frac{K_{pump}}{[Ca^{2+}]_i}}$$

with I_{max} = 2.55 mA/cm^2 and K_{pump} = 0.0069 mM. Intracellular Ca^{2+} was buffered by first-order chemical Ca^{2+} buffer with a total concentration of $[B]_i$ and an equilibrium constant of K_d. Calcium buffering was fast and under the assumption of equilibrium conditions, the relationship between the total and free intracellular calcium concentrations, $[Ca^{2+}]_{i,tot}$ and $[Ca^{2+}]_i$, was given by (Borgdorff, 2002, pg. 27):

$$[Ca^{2+}]_{i,tot} = [Ca^{2+}]_i \frac{[B]_i + K_d + [Ca^{2+}]_i}{K_d + [Ca^{2+}]_i}$$

where $[B]_i$ = 1.562 mM*(V_i^0/V_i), V_i is the intracellular compartment volume, V_i^0 is the intracellular compartment volume at rest and K_d = 0.008 mM.

Volume changes

Volume changes were modelled according to Somjen et al. (2008). The rates of intra- and extracellular volume changes were proportional to the difference in osmotic pressure between the intra- and extracellular compartments and fulfilled the conservation of total volume.

$$\frac{dV_i}{dt} = \Delta$$

$$\frac{dV_o}{dt} = -\Delta$$

where

$$\Delta = \frac{c(\pi_i - \pi_o)}{\tau}$$

$$\pi_i = [Na^+]_i + [K^+]_i + [Cl^-]_i + [Ca^{2+}]_i + [HCO_3^-]_i + [A^-]_i$$

$$\pi_o = [Na^+]_o + [K^+]_o + [Cl^-]_o + [Ca^{2+}]_o + [HCO_3^-]_o + [A^-]_o$$

V_i and V_o are the volumes of the intra- and extracellular compartments and τ = 250 ms. The constant c is introduced for unit conversion and is equal to 1 um^3/mM, hence units of Δ are um^3/ms. The extracellular volume was initially 13.1% of the cellular volume and was allowed to shrink maximally down to 4%. Volume changes affected concentrations but not the total mass of each ion within a compartment. The conservation of mass required additional fluxes:

Intracellular

$$J^i_{X,vol} = -\frac{\Delta}{V_i}[X]_i$$

Extracellular

$$J^{o}_{X,vol} = \frac{\Delta}{V_o}[X]_o$$

Initial ion concentrations

The initial concentrations of $[Na^+]_i$, $[Ca^{2+}]_i$, $[Na^+]_o$, $[K^+]_o$, $[Ca^{2+}]_o$ and $[A^+]_o$ were based on Somjen et al. (2008), and the initial concentration of $[HCO_3^-]_i$ was based on Doyon et al. (2011). Chloride concentrations were set to satisfy the thermodynamic equilibrium of KCC2, i.e., $[Cl^-]_o = [K^+]_i$ and $[Cl^-]_i = [K^+]_o$ giving $E_{Cl} = E_K$. The remaining ions, i.e., $[K^+]_i$, $[A^+]_i$ and $[HCO_3^-]_o$ were solved to fulfil electroneutrality and osmotic equilibrium conditions. Hence, the initial concentrations were as follows (in mM): $[Na^+]_i = 10$, $[Na^-]_o = 140$, $[K^+]_o = 3.5$, $[Ca^{2+}]_i = 5e\text{-}5$, $[Ca^{2+}]_o = 2$, $[A^+]_o = 0$, $[HCO_3^-]_i = 15$, $[K^+]_i = 136.5$, $[A^+]_i = 128$, $[HCO_3^-]_o = 11$, $[Cl^-]_o = 3.5$ and $[Cl^-]_i = 136.5$.

Synaptic connections and model inputs

The pyramidal cells created excitatory AMPA synaptic connections with the interneuron and all other pyramidal cells. The interneuron created an inhibitory $GABA_a$ synaptic connection with each pyramidal cell. Excitatory synapses were placed in the middle of the PY dendrite and the middle of the IN soma. Inhibitory synapses were placed in the middle of the PY soma. The time course of synaptic conductance was modelled with a built-in NEURON mechanism Exp2Syn, implementing a dual exponential function:

$$g = g_{max}\left[\exp\left(-\frac{t}{\tau_2}\right) - \exp\left(-\frac{t}{\tau_1}\right)\right]$$

where the rise and decay time constants, τ_1 and τ_2, were 2 ms and 6 ms, respectively, for all synapses. g_{max} = weight*factor, where the factor was defined so that the normalized peak was 1. The weights for the synapses between the PY and from the PY to the IN were $w_{ee} = 0.0006$ µS and $w_{ei} = 0.001$ µS, respectively. The inhibitory synaptic weight, w_{ie}, was 0.0003 µS. All pyramidal cells received background input modelled as a Poisson spike train, which was different in each cell, activated an excitatory synapse at a rate of 5 Hz and had a synaptic weight $w_{input} = 0.0005$ µS. To initiate the SLE, a depolarizing ramp current, I_{inj}, was injected into the interneuron, with the initial amplitude of 0.8 nA linearly decreasing toward 0 over 30 seconds. The inhibitory $GABA_a$ postsynaptic currents were carried by Cl^- and HCO_3^- ions. The receptor pore conducts Cl^- and HCO_3^- at a ratio of 4:1 (Voipio et al., 1991), hence, E_{GABAa} was calculated as (Doyon et al., 2011):

$$E_{GABAa} = 2.3\frac{RT}{F}\left(\frac{4[Cl^-]_i + [HCO_3^-]_i}{4[Cl^-]_o + [HCO_3^-]_o}\right)$$

HCO_3^- concentrations were assumed to be constant and equal to $[HCO_3^-]_i$ = 15 mM and $[HCO_3^-]_o$ = 11 mM.

Calculation of the LFP

The local field potentials were calculated based on all transmembrane currents in all cells using the following equation (Nunez & Srinivasan, 2006):

$$\phi(r,t) = \frac{1}{4\pi\sigma}\sum_{n=1}^{N}\frac{I_n(t)}{|r - r_n|}$$

Where I_n is a point current source at position r_n (taken as the position of a mid-point of a compartment) and r is the position of the electrode. σ = 0.3 S/m is the extracellular conductivity (Lindén et al., 2014). The electrode was located in the middle of the somatic layer of the PY and IN cells, approximately 16 um from the centers of the somas of two neighbouring PY cells. The currents from the interneuron were taken with a weight of 0.2 to decrease their contribution. Also, the influence of the injected current on the LFP was removed. The amplitude of the simulated LFP signal was an order of magnitude smaller than the experimental data. This was due to current point-source approximation and the small number of cells in the modeled network.

Software Accessibility

If accepted, the model will be publicly available in the ModelDB (https://senselab.med.yale.edu/modeldb/)

Acknowledgements

We are grateful to Laura Uva and Laura Librizzi for helpful discussions throughout the preparation of this work and for providing the SLE data from the *in vitro* isolated whole guinea pig brain. We thank Laura Tassi from the *Claudio Munari* Epilepsy Surgery Center of the Niguarda Hospital in Milano, Italy, for providing the intracerebral data on human seizures. The work of MdC and VG was supported by the EPICARE grant of the Associazione Paolo Zorzi for the Neuroscience.

Competing interests

The authors report no competing interests.

References

Alfonsa, H., Merricks, E. M., Codadu, N. K., Cunningham, M. O., Deisseroth, K., Racca, C., & Trevelyan, A. J. (2015). The Contribution of Raised Intraneuronal Chloride to Epileptic Network Activity. *Journal of Neuroscience*, *35*(20), 7715–7726. https://doi.org/10.1523/JNEUROSCI.4105-14.2015

Aracri, P., de Curtis, M., Forcaia, G., & Uva, L. (2018). Enhanced thalamo-hippocampal synchronization during focal limbic seizures. *Epilepsia*, *59*(9), 1774–1784. https://doi.org/10.1111/epi.14521

Avoli, M., De Curtis, M., Gnatkovsky, V., Gotman, J., Köhling, R., Lévesque, M., Manseau, F., Shiri, Z., & Williams, S. (2016). Specific imbalance of excitatory/inhibitory signaling establishes seizure onset pattern in temporal lobe epilepsy. *Journal of Neurophysiology*, *115*(6), 3229–3237. https://doi.org/10.1152/jn.01128.2015

Bauer, P. R., Thijs, R. D., Lamberts, R. J., Velis, D. N., Visser, G. H., Tolner, E. A., Sander, J. W., Lopes da Silva, F. H., & Kalitzin, S. N. (2017). Dynamics of convulsive seizure termination and postictal generalized EEG suppression. *Brain*, *140*(3), 655–668. https://doi.org/10.1093/brain/aww322

Bazhenov, M., Timofeev, I., Steriade, M., & Sejnowski, T. J. (2004). Potassium model for slow (2-3 Hz) in vivo neocortical paroxysmal oscillations. *Journal of Neurophysiology*, *92*(2), 1116–1132. https://doi.org/10.1152/jn.00529.2003

Blauwblomme, T., Jiruska, P., & Huberfeld, G. (2014). Mechanisms of ictogenesis. In *International Review of Neurobiology* (Vol. 114, pp. 155–185). Academic Press Inc. https://doi.org/10.1016/B978-0-12-418693-4.00007-8

Boido, D., Gnatkovsky, V., Uva, L., Francione, S., & De Curtis, M. (2014). Simultaneous enhancement of excitation and postburst inhibition at the end of focal seizures. *Annals of Neurology*, *76*(6), 826–836. https://doi.org/10.1002/ana.24193

Borgdorff, J. A. (2002). *Calcium dynamics in hippocampal neurones* [University of Amsterdam]. https://hdl.handle.net/11245/1.201021

Bradford, H. F. (1995). Glutamate, GABA and epilepsy. *Progress in Neurobiology*, *47*(6), 477–511. https://doi.org/10.1016/0301-0082(95)00030-5

Bragin, A., Azizyan, A., Almajano, J., & Engel, J. (2009). The Cause of the Imbalance in the Neuronal Network Leading to Seizure Activity Can Be Predicted by the Electrographic Pattern of the Seizure Onset. *Journal of Neuroscience*, *29*(11), 3660–3671. https://doi.org/10.1523/JNEUROSCI.5309-08.2009

Bragin, Anatol, Penttonen, M., & Buzsáki, G. (1997). Termination of Epileptic Afterdischarge in the Hippocampus. *The Journal of Neuroscience*, *17*(7), 2567–2579. https://doi.org/10.1523/JNEUROSCI.17-07-02567.1997

Bromfield, E. B., Cavazos, J. E., & Sirven, J. I. (Eds.). (2006). *An Introduction to Epilepsy [Internet]*. West Hartford (CT): American Epilepsy Society. https://www.ncbi.nlm.nih.gov/books/NBK2508/

Buchin, A., Chizhov, A., Huberfeld, G., Miles, R., & Gutkin, B. S. (2016). Reduced efficacy of the KCC2 cotransporter promotes epileptic oscillations in a subiculum network model. *Journal of Neuroscience*, *36*(46), 11619–11633. https://doi.org/10.1523/JNEUROSCI.4228-15.2016

Chizhov, A. V., Zefirov, A. V., Amakhin, D. V., Smirnova, E. Y., & Zaitsev, A. V. (2018). Minimal model of interictal and ictal discharges "Epileptor-2." *PLoS Computational Biology*, *14*(5), 1–25. https://doi.org/10.1371/journal.pcbi.1006186

Conradsen, I., Moldovan, M., Jennum, P., Wolf, P., Farina, D., & Beniczky, S. (2013). Dynamics of muscle activation during tonic–clonic seizures. *Epilepsy Research*, *104*(1–2), 84–93. https://doi.org/10.1016/j.eplepsyres.2012.09.004

de Curtis, M., & Avoli, M. (2016). GABAergic networks jump-start focal seizures. *Epilepsia*, *57*(5), 679–687. https://doi.org/10.1111/epi.13370

de Curtis, M., & Gnatkovsky, V. (2009). Reevaluating the mechanisms of focal ictogenesis: The role of low-voltage fast activity. *Epilepsia*, *50*(12), 2514–2525. https://doi.org/10.1111/j.1528-1167.2009.02249.x

de Curtis, M., Librizzi, L., & Uva, L. (2006). In Vitro Isolated Guinea Pig Brain. In A. Pitkänen, P. A. Schwartzkroin, & S. L. Moshé (Eds.), *Models of Seizures and Epilepsy* (pp. 103–109). Academic Press Inc. https://doi.org/10.1016/B978-012088554-1/50011-6

de Curtis, M., Uva, L., Gnatkovsky, V., & Librizzi, L. (2018). Potassium dynamics and seizures: Why is potassium ictogenic? *Epilepsy Research*, *143*(April), 50–59. https://doi.org/10.1016/j.eplepsyres.2018.04.005

Derchansky, M., Jahromi, S. S., Mamani, M., Shin, D. S., Sik, A., & Carlen, P. L. (2008). Transition to seizures in the isolated immature mouse hippocampus: a switch from dominant phasic inhibition to dominant phasic excitation. *The Journal of Physiology*, *586*(2), 477–494. https://doi.org/10.1113/jphysiol.2007.143065

Devinsky, O., Vezzani, A., O'Brien, T. J., Jette, N., Scheffer, I. E., de Curtis, M., & Perucca, P. (2018). Epilepsy. *Nature Reviews Disease Primers*, *4*(1), 18024. https://doi.org/10.1038/nrdp.2018.24

Doyon, N., Prescott, S. A., Castonguay, A., Godin, A. G., Kröger, H., & de Koninck, Y. (2011). Efficacy of synaptic inhibition depends on multiple, dynamically interacting mechanisms implicated in chloride homeostasis. *PLoS Computational Biology*, *7*(9). https://doi.org/10.1371/journal.pcbi.1002149

During, M. J., & Spencer, D. D. (1992). Adenosine: A potential mediator of seizure arrest and postictal refractoriness. *Annals of Neurology*, *32*(5), 618–624. https://doi.org/10.1002/ana.410320504

Ebert, U., Cramer, S., & Löscher, W. (1997). Phenytoin's effect on the spread of seizure activity in the amygdala kindling model. *Naunyn-Schmiedeberg's Archives of Pharmacology*, *356*(3), 341–347. https://doi.org/10.1007/PL00005060

Elahian, B., Lado, N. E., Mankin, E., Vangala, S., Misra, A., Moxon, K., Fried, I., Sharan, A., Yeasin, M., Staba, R., Bragin, A., Avoli, M., Sperling, M. R., Engel, J., & Weiss, S. A. (2018). Low-voltage fast seizures in humans begin with increased interneuron firing. *Annals of Neurology*, *84*(4), 588–600. https://doi.org/10.1002/ana.25325

Evangelista, E., Bénar, C., Bonini, F., Carron, R., Colombet, B., Régis, J., & Bartolomei, F.

(2015). Does the Thalamo-Cortical Synchrony Play a Role in Seizure Termination? *Frontiers in Neurology*, *6*. https://doi.org/10.3389/fneur.2015.00192

Feng, Z., & Durand, D. M. (2003). Low-Calcium Epileptiform Activity in the Hippocampus In Vivo. *Journal of Neurophysiology*, *90*(4), 2253–2260. https://doi.org/10.1152/jn.00241.2003

Fisher, R. S., Pedley, T. A., Moody, W. J., & Prince, D. A. (1976). The Role of Extracellular Potassium in Hippocampal Epilepsy. *Archives of Neurology*, *33*(2), 76–83. https://doi.org/10.1001/archneur.1976.00500020004002

Fisher, Robert S., & Schachter, S. C. (2000). The Postictal State: A Neglected Entity in the Management of Epilepsy. *Epilepsy and Behavior*, *1*(1), 52–59. https://doi.org/10.1006/ebeh.2000.0023

Franaszczuk, P. J., Bergey, G. K., Durka, P. J., & Eisenberg, H. M. (1998). Time-frequency analysis using the matching pursuit algorithm applied to seizures originating from the mesial temporal lobe. *Electroencephalography and Clinical Neurophysiology*, *106*(6), 513–521. https://doi.org/10.1016/S0013-4694(98)00024-8

Fransen, E., Alonso, A. A., & Hasselmo, M. E. (2002). Simulations of the role of the muscarinic-activated calcium-sensitive nonspecific cation current INCM in entorhinal neuronal activity during delayed matching tasks. *Journal of Neuroscience*, *22*(3), 1081–1097. https://doi.org/10.1523/jneurosci.22-03-01081.2002

Fröhlich, F., Bazhenov, M., Timofeev, I., Steriade, M., & Sejnowski, T. J. (2006). Slow state transitions of sustained neural oscillations by activity-dependent modulation of intrinsic excitability. *Journal of Neuroscience*, *26*(23), 6153–6162. https://doi.org/10.1523/JNEUROSCI.5509-05.2006

Fujiwara-Tsukamoto, Y., Isomura, Y., Imanishi, M., Fukai, T., & Takada, M. (2007). Distinct types of ionic modulation of GABA actions in pyramidal cells and interneurons during electrical induction of hippocampal seizure-like network activity. *European Journal of Neuroscience*, *25*(9), 2713–2725. https://doi.org/10.1111/j.1460-9568.2007.05543.x

Futamachi, K. J., Mutani, R., & Prince, D. A. (1974). Potassium activity in rabbit cortex. *Brain*

Research, *75*(1), 5–25. https://doi.org/10.1016/0006-8993(74)90767-7

Gentiletti, D., Suffczynski, P., Gnatkovsky, V., & De Curtis, M. (2017). Changes of Ionic Concentrations during Seizure Transitions-A Modeling Study. *International Journal of Neural Systems*, *27*(4), 1–16. https://doi.org/10.1142/S0129065717500046

Gnatkovsky, V., Librizzi, L., Trombin, F., & De Curtis, M. (2008). Fast activity at seizure onset is mediated by inhibitory circuits in the entorhinal cortex in vitro. *Annals of Neurology*, *64*(6), 674–686. https://doi.org/10.1002/ana.21519

Golomb, D., Yue, C., & Yaari, Y. (2006). Contribution of Persistent Na + Current and M-Type K + Current to Somatic Bursting in CA1 Pyramidal Cells: Combined Experimental and Modeling Study. *Journal of Neurophysiology*, *96*(4), 1912–1926. https://doi.org/10.1152/jn.00205.2006

González, O. C., Shiri, Z., Krishnan, G. P., Myers, T. L., Williams, S., Avoli, M., & Bazhenov, M. (2018). Role of KCC2-dependent potassium efflux in 4-Aminopyridine-induced Epileptiform synchronization. *Neurobiology of Disease*, *109*(August 2017), 137–147. https://doi.org/10.1016/j.nbd.2017.10.011

Grasse, D. W., Karunakaran, S., & Moxon, K. A. (2013). Neuronal synchrony and the transition to spontaneous seizures. *Experimental Neurology*, *248*, 72–84. https://doi.org/10.1016/j.expneurol.2013.05.004

Haas, H. L., & Jefferys, J. G. (1984). Low-calcium field burst discharges of CA1 pyramidal neurones in rat hippocampal slices. *The Journal of Physiology*, *354*(1), 185–201. https://doi.org/10.1113/jphysiol.1984.sp015371

Hamidi, S., & Avoli, M. (2015). KCC2 function modulates in vitro ictogenesis. *Neurobiology of Disease*, *79*, 51–58. https://doi.org/10.1016/j.nbd.2015.04.006

Heinemann, U., Lux, H. D., & Gutnick, M. J. (1977). Extracellular free calcium and potassium during paroxysmal activity in the cerebral cortex of the cat. *Experimental Brain Research*, *27*(3–4), 237–243. https://doi.org/10.1007/BF00235500

Heinemann, Uwe, & Lux, H. D. (1975). Undershoots following stimulus-induced rises of

extracellular potassium concentration in cerebral cortex of cat. *Brain Research*, *93*(1), 63–76. https://doi.org/10.1016/0006-8993(75)90286-3

Ho, Y. E. C., & Truccolo, W. (2016). Interaction between synaptic inhibition and glial-potassium dynamics leads to diverse seizure transition modes in biophysical models of human focal seizures. *Journal of Computational Neuroscience*, *41*(2), 225–244. https://doi.org/10.1007/s10827-016-0615-7

Igelström, K. M. (2013). Is Slack an Intrinsic Seizure Terminator? *The Neuroscientist*, *19*(3), 248–254. https://doi.org/10.1177/1073858412446311

Jefferys, J. G. (1995). Nonsynaptic modulation of neuronal activity in the brain: electric currents and extracellular ions. *Physiological Reviews*, *75*(4), 689–723. https://doi.org/10.1152/physrev.1995.75.4.689

Jefferys, J. G. R., & Haas, H. L. (1982). Synchronized bursting of CA1 hippocampal pyramidal cells in the absence of synaptic transmission. *Nature*, *300*(5891), 448–450. https://doi.org/10.1038/300448a0

Jefferys, J., Jiruska, P., de Curtis, M., & Avoli, M. (2012). Limbic Network Synchronization and Temporal Lobe Epilepsy. In J. Noebels, M. Avoli, M. Rogawski, R. Olsen, & A. Delgado-Escueta (Eds.), *Jasper's Basic Mechanisms of the Epilepsies*. Bethesda (MD): National Center for Biotechnology Information (US). http://www.ncbi.nlm.nih.gov/pubmed/22787650

Jensen, M. S., & Yaari, Y. (1997). Role of intrinsic burst firing, potassium accumulation, and electrical coupling in the elevated potassium model of hippocampal epilepsy. *Journal of Neurophysiology*, *77*(3), 1224–1233. https://doi.org/10.1152/jn.1997.77.3.1224

Jirsa, V. K., Stacey, W. C., Quilichini, P. P., Ivanov, A. I., & Bernard, C. (2014). On the nature of seizure dynamics. *Brain*, *137*(8), 2210–2230. https://doi.org/10.1093/brain/awu133

Kager, H., Wadman, W. J., & Somjen, G. G. (2000). Simulated Seizures and Spreading Depression in a Neuron Model Incorporating Interstitial Space and Ion Concentrations. *Journal of Neurophysiology*, *84*(1), 495–512. https://doi.org/10.1152/jn.2000.84.1.495

Kager, H., Wadman, W. J., & Somjen, G. G. (2002). Conditions for the triggering of spreading depression studied with computer simulations. *Journal of Neurophysiology*, *88*(5), 2700–2712. https://doi.org/10.1152/jn.00237.2002

Kaila, K., Price, T. J., Payne, J. A., Puskarjov, M., & Voipio, J. (2014). Cation-chloride cotransporters in neuronal development, plasticity and disease. *Nature Reviews Neuroscience*, *15*(10), 637–654. https://doi.org/10.1038/nrn3819

Kalitzin, S. N., Bauer, P. R., Lamberts, R. J., Velis, D. N., Thijs, R. D., & Da Silva, F. H. L. (2016). Automated Video Detection of Epileptic Convulsion Slowing as a Precursor for Post-Seizure Neuronal Collapse. *International Journal of Neural Systems*, *26*(8), 100–104. https://doi.org/10.1142/S0129065716500271

Krishnan, G. P., & Bazhenov, M. (2011). Ionic dynamics mediate spontaneous termination of seizures and postictal depression state. *Journal of Neuroscience*, *31*(24), 8870–8882. https://doi.org/10.1523/JNEUROSCI.6200-10.2011

Krishnan, G. P., Filatov, G., Shilnikov, A., & Bazhenov, M. (2015). Electrogenic properties of the Na+/K+ ATPase control transitions between normal and pathological brain states. *Journal of Neurophysiology*, *113*(9), 3356–3374. https://doi.org/10.1152/jn.00460.2014

Lado, F. A., & Moshé, S. L. (2008). How do seizures stop? *Epilepsia*, *49*(10), 1651–1664. https://doi.org/10.1111/j.1528-1167.2008.01669.x

Lagarde, S., Buzori, S., Trebuchon, A., Carron, R., Scavarda, D., Milh, M., McGonigal, A., & Bartolomei, F. (2019). The repertoire of seizure onset patterns in human focal epilepsies: Determinants and prognostic values. *Epilepsia*, *60*(1), 85–95. https://doi.org/10.1111/epi.14604

Lévesque, M., Herrington, R., Hamidi, S., & Avoli, M. (2016). Interneurons spark seizure-like activity in the entorhinal cortex. *Neurobiology of Disease*, *87*, 91–101. https://doi.org/10.1016/j.nbd.2015.12.011

Lian, J., Bikson, M., Shuai, J., & Durand, D. M. (2001). Propagation of non-synaptic epileptiform activity across a lesion in rat hippocampal slices. *Journal of Physiology*, *537*(1), 191–199. https://doi.org/10.1111/j.1469-7793.2001.0191k.x

Lillis, K. P., Kramer, M. A., Mertz, J., Staley, K. J., & White, J. A. (2012). Pyramidal cells accumulate chloride at seizure onset. *Neurobiology of Disease*, *47*(3), 358–366. https://doi.org/10.1016/j.nbd.2012.05.016

Lindén, H., Hagen, E., Łeski, S., Norheim, E. S., Pettersen, K. H., & Einevoll, G. T. (2014). LFPy: A tool for biophysical simulation of extracellular potentials generated by detailed model neurons. *Frontiers in Neuroinformatics*, *7*(JAN), 1–15. https://doi.org/10.3389/fninf.2013.00041

Liou, J., Smith, E. H., Bateman, L. M., Bruce, S. L., McKhann, G. M., Goodman, R. R., Emerson, R. G., Schevon, C. A., & Abbott, L. (2020). A model for focal seizure onset, propagation, evolution, and progression. *ELife*, *9*. https://doi.org/10.7554/eLife.50927

Lopantsev, V., & Avoli, M. (1998). Participation of GABA(A)-mediated inhibition in ictallike discharges in the rat entorhinal cortex. *Journal of Neurophysiology*, *79*(1), 352–360. https://doi.org/10.1152/jn.1998.79.1.352

Magistretti, J., & Alonso, A. (1999). Biophysical Properties and Slow Voltage-Dependent Inactivation of a Sustained Sodium Current in Entorhinal Cortex Layer-II Principal Neurons. *Journal of General Physiology*, *114*(4), 491–509. https://doi.org/10.1085/jgp.114.4.491

Magloire, V., Cornford, J., Lieb, A., Kullmann, D. M., & Pavlov, I. (2019). KCC2 overexpression prevents the paradoxical seizure-promoting action of somatic inhibition. *Nature Communications*, *10*(1), 1–13. https://doi.org/10.1038/s41467-019-08933-4

Martinet, L.-E., Fiddyment, G., Madsen, J. R., Eskandar, E. N., Truccolo, W., Eden, U. T., Cash, S. S., & Kramer, M. A. (2017). Human seizures couple across spatial scales through travelling wave dynamics. *Nature Communications*, *8*(1), 14896. https://doi.org/10.1038/ncomms14896

McBain, C., Traynelis, S., & Dingledine, R. (1990). Regional variation of extracellular space in the hippocampus. *Science*, *249*(4969), 674–677. https://doi.org/10.1126/science.2382142

Miri, M. L., Vinck, M., Pant, R., & Cardin, J. A. (2018). Altered hippocampal interneuron

activity precedes ictal onset. *ELife*, *7*. https://doi.org/10.7554/eLife.40750

Moore, Y. E., Deeb, T. Z., Chadchankar, H., Brandon, N. J., & Moss, S. J. (2018). Potentiating KCC2 activity is sufficient to limit the onset and severity of seizures. *Proceedings of the National Academy of Sciences of the United States of America*, *115*(40), 10166–10171. https://doi.org/10.1073/pnas.1810134115

Nunez, P. L., & Srinivasan, R. (2006). *Electric Fields of the Brain*. Oxford University Press. https://doi.org/10.1093/acprof:oso/9780195050387.001.0001

Payne, D. E., Karoly, P. J., Freestone, D. R., Boston, R., D'Souza, W., Nurse, E., Kuhlmann, L., Cook, M. J., & Grayden, D. B. (2018). Postictal suppression and seizure durations: A patient-specific, long-term iEEG analysis. *Epilepsia*, *59*(5), 1027–1036. https://doi.org/10.1111/epi.14065

Payne, J. A. (1997). Functional characterization of the neuronal-specific K-Cl cotransporter: Implications for [K+](o) regulation. *American Journal of Physiology - Cell Physiology*, *273*(5 42-5). https://doi.org/10.1152/ajpcell.1997.273.5.c1516

Payne, J. A., Rivera, C., Voipio, J., & Kaila, K. (2003). Cation-chloride co-transporters in neuronal communication, development and trauma. *Trends in Neurosciences*, *26*(4), 199–206. https://doi.org/10.1016/S0166-2236(03)00068-7

Perucca, P., Dubeau, F., & Gotman, J. (2014). Intracranial electroencephalographic seizure-onset patterns: effect of underlying pathology. *Brain*, *137*(1), 183–196. https://doi.org/10.1093/brain/awt299

Pottkämper, J. C. M., Hofmeijer, J., van Waarde, J. A., & van Putten, M. J. A. M. (2020). The postictal state — What do we know? *Epilepsia*, *61*(6), 1045–1061. https://doi.org/10.1111/epi.16519

Proix, T., Jirsa, V. K., Bartolomei, F., Guye, M., & Truccolo, W. (2018). Predicting the spatiotemporal diversity of seizure propagation and termination in human focal epilepsy. *Nature Communications*, *9*(1), 1088. https://doi.org/10.1038/s41467-018-02973-y

Pumain, R., Menini, C., Heinemann, U., Louvel, J., & Silva-Barrat, C. (1985). Chemical

synaptic transmission is not necessary for epileptic seizures to persist in the baboon Papio papio. *Experimental Neurology*, *89*(1), 250–258. https://doi.org/10.1016/0014-4886(85)90280-8

Raimondo, J. V., Burman, R. J., Katz, A. A., & Akerman, C. J. (2015). Ion dynamics during seizures. *Frontiers in Cellular Neuroscience*, *9*, 1–14. https://doi.org/10.3389/fncel.2015.00419

Saggio, M. L., Crisp, D., Scott, J. M., Karoly, P., Kuhlmann, L., Nakatani, M., Murai, T., Dümpelmann, M., Schulze-Bonhage, A., Ikeda, A., Cook, M., Gliske, S. V, Lin, J., Bernard, C., Jirsa, V., & Stacey, W. C. (2020). A taxonomy of seizure dynamotypes. *ELife*, *9*. https://doi.org/10.7554/eLife.55632

Schiff, S. J., Colella, D., Jacyna, G. M., Hughes, E., Creekmore, J. W., Marshall, A., Bozek-Kuzmicki, M., Benke, G., Gaillard, W. D., Conry, J., & Weinstein, S. R. (2000). Brain chirps: spectrographic signatures of epileptic seizures. *Clinical Neurophysiology*, *111*(6), 953–958. https://doi.org/10.1016/S1388-2457(00)00259-5

Schindler, K., Leung, H., Elger, C. E., & Lehnertz, K. (2007). Assessing seizure dynamics by analysing the correlation structure of multichannel intracranial EEG. *Brain*, *130*(1), 65–77. https://doi.org/10.1093/brain/awl304

Shivacharan, R. S., Chiang, C.-C., Zhang, M., Gonzalez-Reyes, L. E., & Durand, D. M. (2019). Self-propagating, non-synaptic epileptiform activity recruits neurons by endogenous electric fields. *Experimental Neurology*, *317*, 119–128. https://doi.org/10.1016/j.expneurol.2019.02.005

Somjen, G. G., Kager, H., & Wadman, W. J. (2008). Computer simulations of neuron-glia interactions mediated by ion flux. *Journal of Computational Neuroscience*, *25*(2), 349–365. https://doi.org/10.1007/s10827-008-0083-9

Spencer, S. S., Guimaraes, P., Katz, A., Kim, J., & Spencer, D. (1992). Morphological Patterns of Seizures Recorded Intracranially. *Epilepsia*, *33*(3), 537–545. https://doi.org/10.1111/j.1528-1157.1992.tb01706.x

Suffczynski, P., Gentiletti, D., Gnatkovsky, V., & de Curtis, M. (2017). Extracellular

Potassium and Focal Seizures—Insight from In Silico Study. In P. Érdi, B. Sen Bhattacharya, & A. Cochran (Eds.), *Computational Neurology and Psychiatry. Springer Series in Bio-/Neuroinformatics* (pp. 49–72). Springer, Cham. https://doi.org/10.1007/978-3-319-49959-8_3

Thompson, S. M., & Gahwiler, B. H. (1989). Activity-dependent disinhibition. II. Effects of extracellular potassium, furosemide, and membrane potential on ECl- in hippocampal CA3 neurons. *Journal of Neurophysiology*, *61*(3), 512–523. https://doi.org/10.1152/jn.1989.61.3.512

Timofeev, I., & Steriade, M. (2004). Neocortical seizures: initiation, development and cessation. *Neuroscience*, *123*(2), 299–336. https://doi.org/10.1016/j.neuroscience.2003.08.051

Toyoda, I., Fujita, S., Thamattoor, A. K., & Buckmaster, P. S. (2015). Unit activity of hippocampal interneurons before spontaneous seizures in an animal model of temporal lobe epilepsy. *Journal of Neuroscience*, *35*(16), 6600–6618. https://doi.org/10.1523/JNEUROSCI.4786-14.2015

Traub, R. D., Buhl, E. H., Gloveli, T., & Whittington, M. A. (2003). Fast Rhythmic Bursting Can Be Induced in Layer 2/3 Cortical Neurons by Enhancing Persistent Na + Conductance or by Blocking BK Channels. *Journal of Neurophysiology*, *89*(2), 909–921. https://doi.org/10.1152/jn.00573.2002

Truccolo, W., Donoghue, J. A., Hochberg, L. R., Eskandar, E. N., Madsen, J. R., Anderson, W. S., Brown, E. N., Halgren, E., & Cash, S. S. (2011). Single-neuron dynamics in human focal epilepsy. *Nature Neuroscience*, *14*(5), 635–643. https://doi.org/10.1038/nn.2782

Uva, L., Breschi, G. L., Gnatkovsky, V., Taverna, S., & de Curtis, M. (2015). Synchronous inhibitory potentials precede seizure-like events in acute models of focal limbic seizures. *Journal of Neuroscience*, *35*(7), 3048–3055. https://doi.org/10.1523/JNEUROSCI.3692-14.2015

Uva, L., & de Curtis, M. (2020). Activity- and pH-dependent adenosine shifts at the end of a focal seizure in the entorhinal cortex. *Epilepsy Research*, *165*, 106401. https://doi.org/10.1016/j.eplepsyres.2020.106401

Velascol, A. L., Wilson, C. L., Babb, T. L., & Engel Jr, J. (2000). Functional and Anatomic Correlates of Two Frequently Observed Temporal Lobe Seizure-Onset Patterns. *Neural Plasticity*, *7*(1–2), 49–63. https://doi.org/10.1155/NP.2000.49

Viitanen, T., Ruusuvuori, E., Kaila, K., & Voipio, J. (2010). The K+-Cl- cotransporter KCC2 promotes GABAergic excitation in the mature rat hippocampus. *Journal of Physiology*, *588*(9), 1527–1540. https://doi.org/10.1113/jphysiol.2009.181826

Voipio, J., Pasternack, M., Rydqvist, B., & Kaila, K. (1991). Effect of gamma-aminobutyric acid on intracellular pH in the crayfish stretch-receptor neurone. *The Journal of Experimental Biology*, *156*, 349–360. http://www.ncbi.nlm.nih.gov/pubmed/1711091

Wei, Y., Ullah, G., & Schiff, S. J. (2014). Unification of neuronal spikes, seizures, and spreading depression. *Journal of Neuroscience*, *34*(35), 11733–11743. https://doi.org/10.1523/JNEUROSCI.0516-14.2014

Wen, B., Qian, H., Feng, J., Ge, R.-J., Xu, X., Cui, Z.-Q., Zhu, R.-Y., Pan, L.-S., Lin, Z.-P., & Wang, J.-H. (2015). A Portion of Inhibitory Neurons in Human Temporal Lobe Epilepsy are Functionally Upregulated: An Endogenous Mechanism for Seizure Termination. *CNS Neuroscience & Therapeutics*, *21*(2), 204–214. https://doi.org/10.1111/cns.12336

Yaari, Y., Konnerth, A., & Heinemann, U. (1983). Spontaneous epileptiform activity of ca1 hippocampal neurons in low extracellular calcium solutions. *Experimental Brain Research*, *51*(1). https://doi.org/10.1007/BF00236813

Ziburkus, J., Cressman, J. R., Barreto, E., & Schiff, S. J. (2006). Interneuron and pyramidal cell interplay during in vitro seizure-like events. *Journal of Neurophysiology*, *95*(6), 3948–3954. https://doi.org/10.1152/jn.01378.2005

Ziemann, A. E., Schnizler, M. K., Albert, G. W., Severson, M. A., Howard III, M. A., Welsh, M. J., & Wemmie, J. A. (2008). Seizure termination by acidosis depends on ASIC1a. *Nature Neuroscience*, *11*(7), 816–822. https://doi.org/10.1038/nn.2132

Zubler, F., Steimer, A., Gast, H., & Schindler, K. A. (2014). Seizure Termination. In *International Review of Neurobiology* (pp. 187–207). Academic Press Inc. https://doi.org/10.1016/B978-0-12-418693-4.00008-X

Supplementary figures

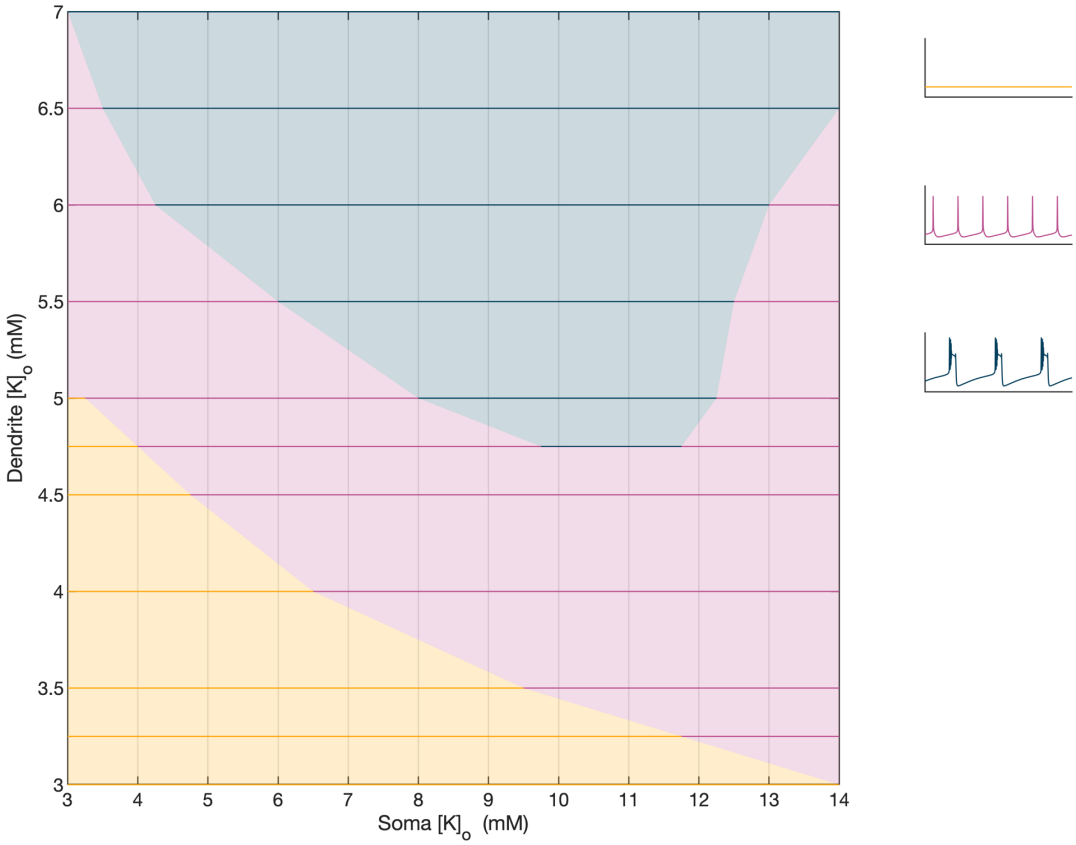

Figure S1. Bifurcation diagram of a single PY cell. The 2D bifurcation diagram demonstrates the behavior of a single PY cell as a function of extracellular potassium concentration in the dendritic ($[K^+]_{o,dend}$) and somatic compartments ($[K^+]_{o,soma}$) used as control parameters. Concentrations of all other ions were fixed at their reference values, all ion accumulation mechanisms were blocked and all synaptic connections were removed. The legend on the right shows the PY cell activity traces for different values of the control parameters: resting (yellow, $[K^+]_{o,soma} = 4$ mM, $[K^+]_{o,dend} = 4$ mM), tonic firing (violet, $[K^+]_{o,soma} = 4$ mM, $[K^+]_{o,dend} = 6$ mM) and bursting (dark blue, $[K^+]_{o,soma} = 6$ mM, $[K^+]_{o,dend} = 6$ mM). In each panel, 2 seconds of activity is shown. The colors of the 2D diagram correspond to the types of activity shown in the

legend. For low $[K^+]_{o,dend}$ and $[K^+]_{o,soma}$ the cell was at rest. A moderate increase in either $[K^+]_{o,dend}$ or $[K^+]_{o,soma}$, or both, led to tonic firing. Subsequent increases in these parameters led to bursting.

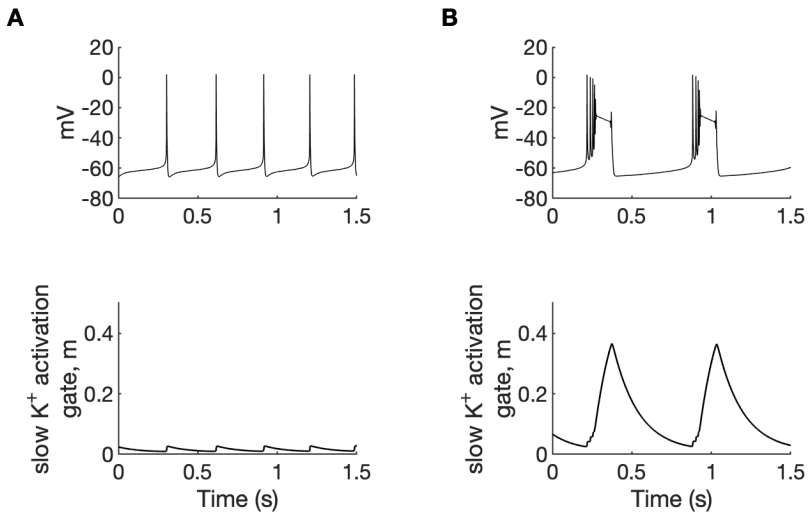

Figure S2. A comparison of tonic firing (A) and bursting (B) of a PY cell. In each column, the membrane potential of a cell (top) and the activation gate of I_{KM} (bottom) is shown. During tonic firing, the activation gate of the M-type potassium current was closed. The prolonged depolarization of the cell during bursting led to the opening of the activation gate *m* and activation of the I_{KM} current, which eventually terminated the burst. The simulation was performed using an isolated PY cell model with the concentrations of all ions fixed at their reference values, except for A: $[K^+]_{o,soma}$ = 11 mM, $[K^+]_{o,dend}$ = 3.75 mM, B: $[K^+]_{o,soma}$ = 11 mM and $[K^+]_{o,dend}$ = 5 mM.